



Effect of Thermal Pre-treatment on Thermal Gradient Response of Granitic Rocks: Insights from Optical Microscopy and Digital Image Correlation

Kareem Ramzy Aboyanah¹ · Ekaterina Ossetchkina¹ · Aly Abdelaziz¹ · Lei Sun^{1,2}  · Karl Peterson¹ · Giovanni Grasselli¹

Received: 10 January 2024 / Accepted: 5 August 2024

© The Author(s), under exclusive licence to Springer-Verlag GmbH Austria, part of Springer Nature 2024

Abstract

Thermal loading history and the induced cracks affect the thermomechanical response of the rock. This paper experimentally investigates, through a staged thermal loading process, the influence of uniform thermal pre-treatment on the following gradient heating responses of Stanstead granite. Specifically, petrographic analysis of thin sections acted as a control test to quantify the crack density and aperture evolution after uniform thermal pre-treatment with various target temperatures. Then, DIC technique was used to investigate the real-time thermomechanical response of the thermally pre-treated samples to thermal gradient loading. Results show that thermal cracks density and aperture increased with the pre-treating temperature, which then significantly affect the thermal cracking pattern under following gradient heating process. During thermal gradient loading, radial pattern of thermal gradient cracking initiating close to the heating source while the macroscopic cracking coalesced from the microcracks at the sample periphery and propagated towards the hotter interior. Interestingly, the results also suggest a transition in the thermomechanical behavior of the Stanstead granite between 300 and 500 °C. Macroscopic cracking was observed in all samples pre-treated at temperatures below 400 °C, while for those pre-treated at higher temperatures, no macroscopic cracking was observed, suggesting that the thermal resistance of the investigated samples increased with increased initial damage under thermal pre-treatment. Mineral grains expansion into pre-existing microcracks during the heating stage was captured using DIC and found to contribute to this behavior. This paper provides useful insights into the effect of the initial crack density and aperture induced by different thermal and/or mechanical loading history on the thermomechanical behavior of granitic rock under in situ temperature variation that might result from a variety of underground applications.

Highlights

- Quantitative analysis of the crack density and aperture evolution under uniform thermal treatment from petrographic images.
- Experimental staged heating treatment to investigate the effect of uniform thermal pre-treatment on thermal gradient response in granite.
- Digital image correlation (DIC) was used to investigate real-time thermomechanical behavior of granite exposed to thermal gradient loading.
- Thermal resistance of granitic rocks to thermal shock increased with increasing pre-existing crack density and aperture.

✉ Lei Sun
leo.sun@mail.utoronto.ca

¹ Department of Civil and Mineral Engineering, University of Toronto, Toronto, Canada

² School of Civil Engineering, Wuhan University, Wuhan, China

Keywords Thermal pre-treatment · Thermal gradient · Initial crack density · Thermomechanical behavior · Digital image correlation (DIC)

1 Introduction

Thermal loading of crustal rocks widely exists in natural activities such as volcanic activity and magma migration due to tectonic movement (Gunatilake 2023; Johnson et al. 2021; Olive and Crone 2018; Veloso et al. 2020), or in anthropogenic activities such as in-situ combustion enhanced oil recovery, geothermal energy exploitation, nuclear waste storage, and microwave assisted rock cracking (Chen et al. 2021; Hassani et al. 2016, 2020; Izadi and Elsworth 2015; Liu et al. 2023; Mahinpey et al. 2007; Mokheimer et al. 2018; Zhang et al. 2019). Thermal loading entails extensive microcracking in rocks when the thermally induced stresses exceed the material's strength. More specifically, thermal cracking is the result of localized stress concentrations caused by the anisotropic thermal expansion of monomineralic substance, the varying thermal expansion of different minerals in polymineralic substance (Fredrich and Wong 1986; Aboyanah et al. 2022), or inhomogeneous strain produced by large thermal gradient (Cooper and Simmons 1977; Sun et al. 2020). Thermal cracking can have favorable effects such as lowering fracture breakdown pressure and branching fracture networks during hydraulic stimulation operations (Feng et al. 2020; Li et al. 2021a; Xue et al. 2023; Zhou et al. 2018), or unfavorable effects such as induced seismicity and lower heating extraction efficiency (Gaucher et al. 2015; Izadi and Elsworth 2015; Martínez-Garzón et al. 2014), deserving more consideration in practical underground engineering.

Thermal loading and thermal cracking in rocks have been experimentally investigated through post-loading techniques and real-time monitoring techniques. Post-loading analysis techniques of thermally treated samples typically include thermal crack density and aperture quantification using thin sections petrographic analysis (Chen et al. 2021; Freire-Lista et al. 2016; Gautam et al. 2022; Li et al. 2020; Nasserri et al. 2007; Sun et al. 2015; Yang 2022) and scanning electron microscopy (Nasserri et al. 2007). Additionally, for granitic rocks the effects of temperature on the uniaxial compressive strength (Wang and Konietzky 2019; Wong et al. 2020), fracture toughness (Nasserri et al. 2009; Shao et al. 2022), Brazilian tensile strength (Li et al. 2017), and dynamic behavior (Fan et al. 2017) have been investigated. The results of these experiments generally reveal weakening effects associated with treating temperatures in excess of 300–400 °C and strengthening or weakening behavior at milder temperatures (< 300 °C). Real-time monitoring techniques during thermal loading, including monitoring of acoustic emission signals

(Browning et al. 2016; Griffiths et al. 2018; Jansen et al. 1993), ultrasound velocity propagation (Griffiths et al. 2018; Wang et al. 2021), X-ray computed tomography (Fan et al. 2018; Guo et al. 2017), digital image correlation (Wang et al. 2020), and mercury intrusion porosimetry (Wu et al. 2021), have been adopted to describe mesoscopic thermal cracking evolution. Recently, Xu et al. (2023) observed thermal microcracking at the grain scale in real-time using optical microscope equipped with ultrahigh temperature capability (up to 900 °C). Jansen et al. (1993) and Glover et al. (1995) observed an onset of acoustic emissions (AE) activity when granite is heated at around 80 °C, while Kong et al. (2018) also reported an increase in AE count during heat treatment of granite between 150 and 200 °C.

In some cases, the real-time monitoring and post-loading analysis supplement each other. In Westerly granite, for example, Glover et al. (1995) through real-time monitoring observed a spike in AE activity at 573 °C. The post-treatment findings of Nasserri et al. (2007), using optical microscopy analysis of thin sections, showed that there is an increase in the number and apertures of microcracks between 450 and 650 °C. Hence, the α - β phase transition of quartz grains at around 573 °C was regarded as the main reason for the accelerated cracking rate and increased crack aperture. In addition, studies have found that in cyclical heating and cooling of granitic rocks, thermal cracking intensity decreases from a maximum in the first cycle to lower intensity in the subsequent cycles (Griffiths et al. 2018; Thirumalai and Demou 1974; Todd 1973; Yong and Wang 1980).

Majority of the studies investigating thermomechanical behavior of rocks independently focused on: (1) cyclic heating using low heating rate to avoid thermal gradient (Freire-Lista et al. 2016; Griffiths et al. 2018; Nasserri et al. 2007; Xu et al. 2023), and (2) thermal shock loading using high thermal gradients (Rossi et al. 2018; Wang et al. 2019, 2020; Yuan et al. 2023; Zhang et al. 2023). However, studies investigating thermomechanical behavior of rocks subjected to staged thermal loading (i.e., uniform heating followed by thermal gradient or shock heating) and the effect of thermal pre-treatment on the following heating responses are rare. Different micromechanical phenomena including increased thermal microcracks density and aperture, escape of bond water, and deteriorating mechanical and thermal properties of the minerals forming the rock appear to control its emerging behavior (Abdelaziz and Grasselli 2018; Aboyanah et al. 2022; Jin et al. 2019; Mo et al. 2022; Xu et al. 2023). Investigating these pre-treated granitic samples further exposed to thermal gradient loading will provide invaluable

insights on the impacts of thermal loading history and the induced crack density and aperture on the thermomechanical response of the rock.

In this research, we aim to fill this knowledge gap using petrographic analysis of thin section images and real-time digital image correlation (DIC) monitoring of thermal gradient loading of granitic rocks uniformly thermally pre-treated to various temperatures. This paper commences with petrographic investigation of the effect of uniform heat treatment on crack density and aperture evolution in Stanstead granite using thin section analysis. An algorithm quantifying crack density and aperture from thin sections is introduced followed by microcracks quantification results. Then, thermal gradient loading of the uniformly thermally pre-treated granitic samples at various temperatures was investigated by means of the digital image correlation (DIC) method. After that, results are discussed in the context of underground applications, followed by the conclusions.

2 Methodology

To investigate the effects of uniform thermal pre-treatment and the consequent crack density and aperture on the thermomechanical response of granite under thermal gradient loading, we designed a staged heating experiment that consists of uniform thermal pre-treatment of Stanstead granite samples to different temperatures followed by thermal gradient loading. Thin section analysis of the pre-treated samples was used as a control test to quantify the crack density and aperture as well as to provide valuable information on the microstructure of the material such as grain size and mineralogical composition. The DIC method was implemented to investigate the thermal gradient loading.

2.1 Samples Preparation and Testing Procedure

Two groups of Stanstead granite were prepared (Fig. 1): Group-1 comprised seven sets (three samples per set, i.e., a total of 21 samples) of 50.0-mm diameter and 25.0-mm thick discs (with a 6.5-mm diameter through-hole at the center) for thermal gradient experimentation with DIC while Group-2 comprised five sets (one sample each) of 25.0-mm diameter and 50.0-mm long cylindrical samples which were used as control samples for thin sections and petrographic analysis. The samples were cored from large outcrop block and cut using a water-cooled precision saw. Following this, the circular surfaces of Group-1 samples were polished using a high precision grinding machine. The samples were then put in an oven at 40 °C for 24 h to dry out prior to the heat treatment.

The heating procedure was divided in two stages: (1) The first stage was the “uniform thermal pre-treatment”

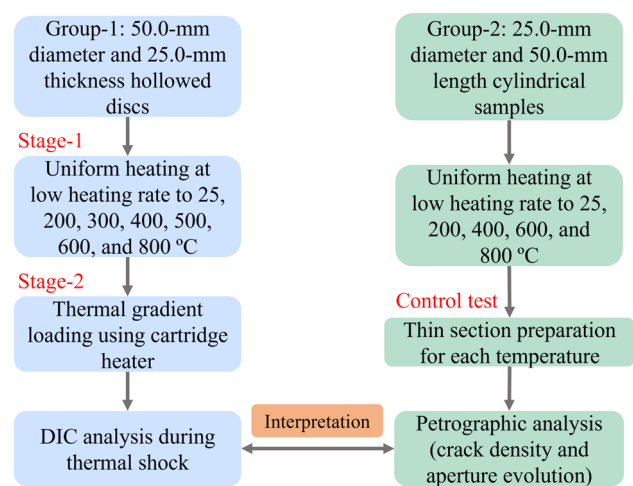
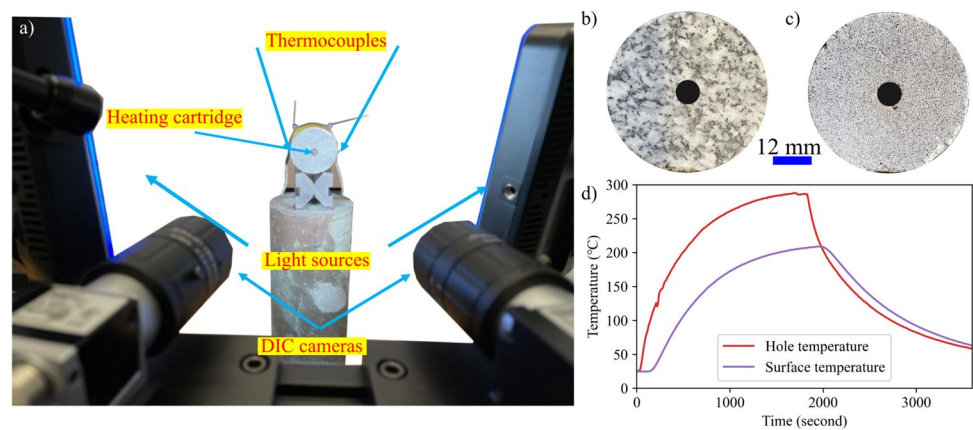


Fig. 1 Workflow of the staged heating experiment adopted in this research

where each set of the seven sets in Group-1 was heated to 25, 200, 300, 400, 500, 600, and 800 °C, respectively, while the five sets in Group-2 were heated to 25, 200, 400, 600, and 800 °C, respectively. The uniform thermal pre-treatment was achieved by placing the samples in an oven and applying a low heating rate of 7 °C/min (Wang and Konietzky 2020; Wang et al. 2020) until the prescribed temperature was achieved and was then maintained for 2 h to ensure temperature equilibrium within the sample. The oven was then turned off and the samples were left in the oven overnight to cool down to room temperature. Due to the thermal insulation of the oven, the gradual cooling of the samples to room temperature effectively prevented thermal shocks following the heat treatment process. The Group-2 samples were then kept aside for thin section preparation to analyse the microcracks caused by the uniform thermal pre-treatment. (2) The second stage comprised of the “thermal gradient loading” and was only performed on the uniform thermally pre-treated Group-1 samples. It is noteworthy that samples uniformly heated to 300 and 500 °C were added later to Group-1 to have better resolution of the thermomechanical behavior of the tested rock, therefore, no thin sections prepared for these samples. Samples were sprayed with a thin layer of black-on-white heat-resistant spray to form speckle patterns for the thermomechanical deformation to be tracked using DIC (Fig. 2b, c). Thermal gradient loading was then applied to the central hole of the disc sample for 60.0 min, more specifically 30.0 min for heating and 30.0 min for cooling (Fig. 2d), using a 6.35-mm diameter heating cartridge. The small clearance in diameter between the cartridge (6.35-mm) and the center hole (6.5-mm) allowed for the accommodation of the thermal expansion of the cartridge and eliminated any potential mechanical stress exerted by the cartridge’s expansion on the disc samples. The heating of

Fig. 2 **a** DIC experimental setup, **b** stanstead granite disc sample with the drilled through-hole and polished prior to applying the speckles spray painting, **c** sample after spray painting, and **d** temperature profile evolution at the sample hole and perimeter



30 min ensured that the maximum hole temperature was in the range from 290 to 300 °C (i.e., the thermal shock applied to Group-1 samples was about 300 °C) (Fig. 2d), lying in the mild temperature range relevant to many underground conditions (Wong et al. 2020). Two thermocouples were used to record the temperature evolution close to the sample hole and its perimeter to provide insights on the heat diffusion inside the sample (Fig. 2a), and a three-dimensional DIC system was set up to capture the real-time thermomechanical deformation of the disc samples at a frequency of 1 frame per second.

2.2 Thin Section Preparation and Petrographic Analysis

Each sample in Group-2 was cut parallel to the circular cross-section using a thin saw blade to minimize induced cracking not related to those induced from the thermal pre-treatment. Billets were then extracted using a thin saw blade at a slow feed rate to mitigate cracking and conserve the

structural stability of the sample. After this, the billets were epoxy-impregnated under 0.2 MPa vacuum pressure, with Tigris Yellow DayGlo fluorescent dye additive, to provide stability for the grains weakened by heat treatment and ensure that the dye percolated into all the fractures and voids in the sample. The billets were ground using a fine diamond grinder before being epoxy impregnated for a second time to stabilize the mineral grains from plucking and to improve the surface finish for high quality microscopy imaging. High resolution images of the thin sections were captured using a BH-2 Olympus optical microscope fitted with an overhead camera having a resolution of 1392 × 1040 pixels which captured images of transmitted light through the sample. Grid images of the thin sections were captured with a twenty percent overlap between successive images to cover the entire surface area of the thin sections at sufficient magnification to observe mineral grains and microcracks. Images were captured under plane-polarized (PPL), crossed-polarized (XPL), and fluorescent light (FLO) using the same procedure. The images of each sample were stitched together to

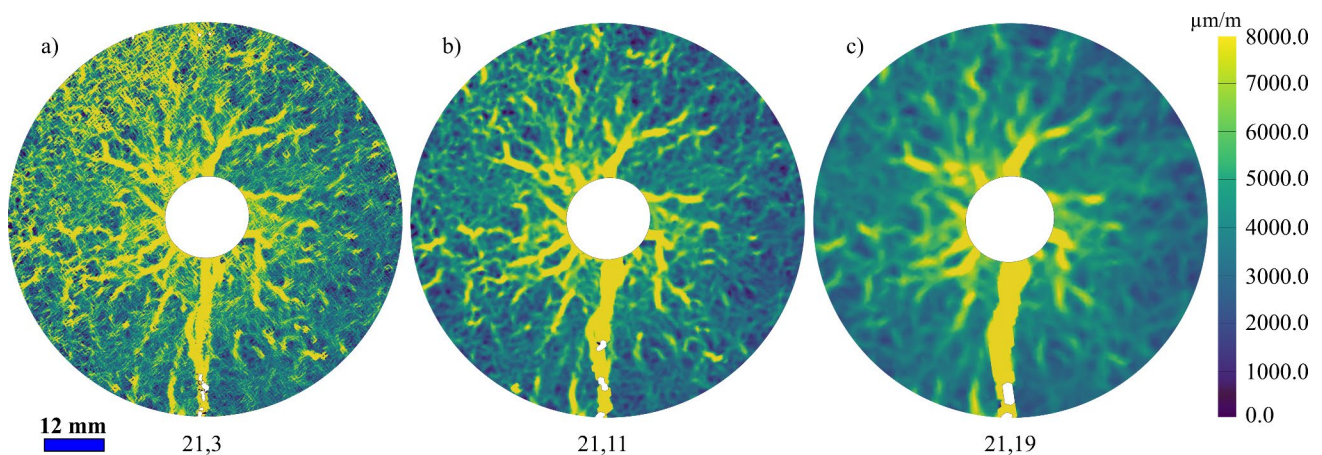


Fig. 3 Effect of step size on the major principal strain field calculations. Step sizes are **a** 3, **b** 11, and **c** 19 pixels for a subset size of 21 pixels. White spots in the pictures apart from the hole are missing subsets

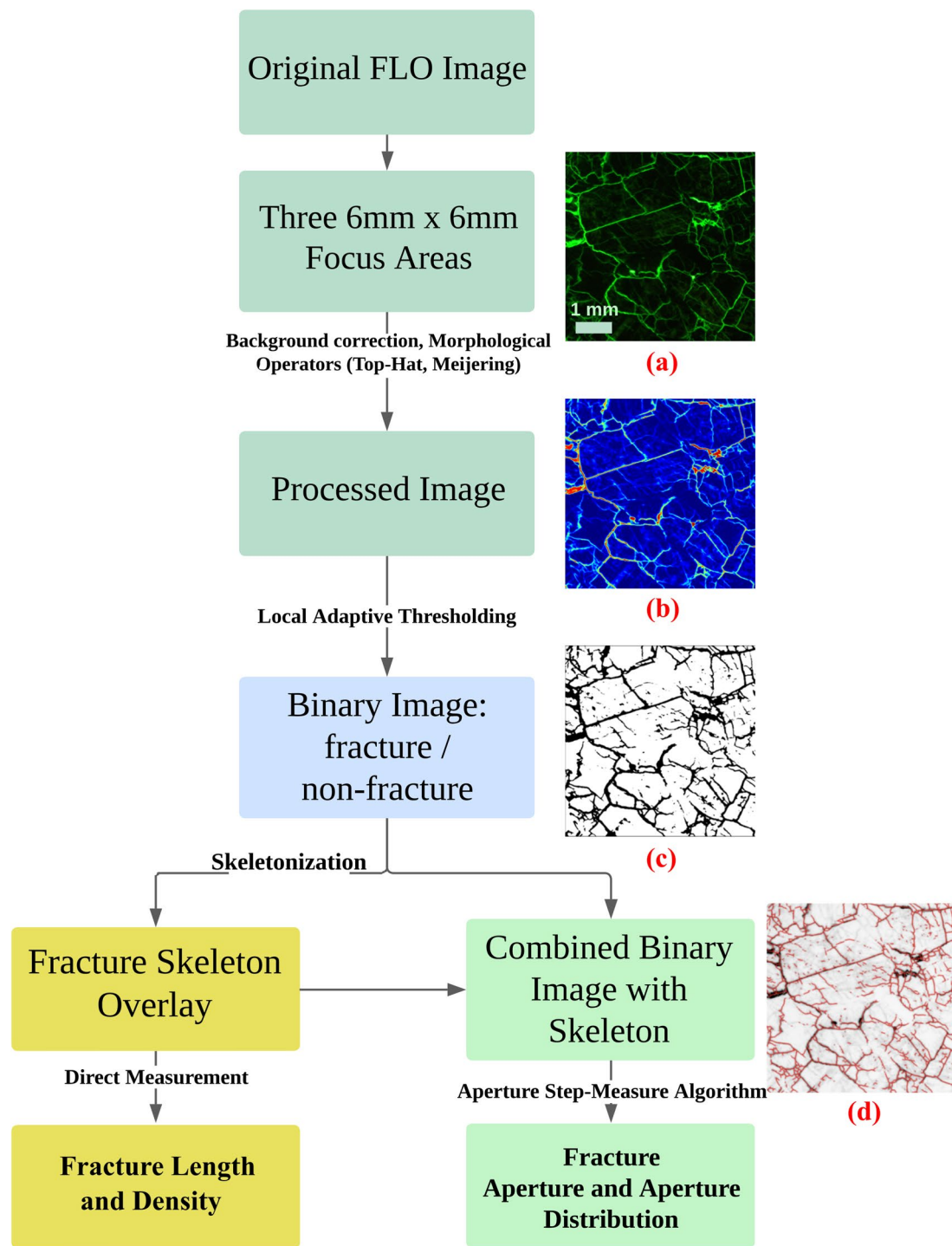


Fig. 4 Microcrack density and aperture quantification workflow with a sample 6.0-mm×6.0-mm representative focus area displaying image pre-processing techniques to separate fracture network. **a** Raw FLO image of the focus area, **b** pre-processed fracture area, with heat

map displaying variation in fracture aperture, **c** binary mask to differentiate fracture network from background, and **d** fracture network (skeleton) overlaid on XPL image

obtain composite images of the entire thin section using the open-source ImageJ v2.1.0/1.53c software (Preibisch et al. 2009). Complete sets of PPL, XPL, and FLO images provided information pertaining to the composition and distribution of mineral grains in the Stanstead granite, as well as the post thermal pre-treatment microcrack networks.

2.3 Thermal Gradient Cracking Testing with DIC

Group-1 samples involved gradient heating which was monitored using digital image correlation (DIC). DIC is a relatively new experimental technique that has been used to study the mechanical behavior of rocks (Abdelaziz et al. 2023; Aboyanah et al. 2024; Dong et al. 2017; Dutler et al. 2018; Lin and Labuz 2013; Lin et al. 2014; Wu et al. 2020; Yu et al. 2020) and can be described as a form of the particle tracking approach, where the displacement vector of a group of particles (called speckles) is tracked (Belrhiti et al. 2012). This group of speckles has a unique speckles intensity pattern, called the “subset”. The setup used herein was a three-dimensional DIC (two Basler acA2500–60um cameras in stereo setup) system used to capture the deformation on one face of the disc samples (Fig. 2a). The cameras recorded digital images of the sample surface sprayed with speckles pattern and a cross-correlation algorithm was employed to calculate the deformation between the reference, i.e., the first captured image, and the successive images. The cross-correlation between the images was achieved using GOM Correlate Pro software. Specifically, crack opening and sliding displacements were calculated from GOM Correlate Pro output using a stand-alone post-processing script written in Python3 (Van Rossum and Drake 2009). Distance between the centers of two adjacent subsets, called step size, has pronounced ramifications on the strain calculation and the width of strain localization which represents the cracks. Based on outputs, a step size of 11 pixels showed a good balance between resolution, noise level, and computational

cost (Fig. 3). In this work, subset and step sizes of 20 and 11 pixels, respectively, were used in the calculations.

To validate the DIC strain field measurement, a 25.0-mm diameter aluminium 6061 (Al) sample heat-treated to a T6 temper was uniaxially loaded using a Forney test frame. A pressure transducer (Ashcroft GV 3000 psi) mounted on the test frame was used to capture the axial load and a high-precision pressure metering pump (Vindum VP-6K) was used to regulate the pressure. Axial strain evolution from the DIC was recorded and averaged from two 5.0-mm axial virtual strain gauges placed on the middle of the sample. The calculated elastic modulus of the aluminum sample from the DIC was 69.5 GPa which agrees well with the theoretical elastic modulus of 69.7 GPa (ASM 1990). Hence, confirming the applicability of the DIC in capturing the proper strain magnitudes.

3 Data Quantification

3.1 Crack Density and Aperture Quantification from Thin Sections

For each of the thin section images of the samples in Group-2, three 6.0-mm × 6.0-mm representative focus areas were selected for crack density and aperture calculation. The following image processing techniques were applied to automatically detect, adjust, and standardize the fracture features and network from the FLO images, to account for the increasing light intensity (from the denser fracture network) in the FLO images at higher temperatures (Fig. 4): (1) The green channel was isolated for further processing; (2) A bilateral blur filter was applied to reduce background noise in the images, by replacing the colour intensity of the pixel with the weighted average of the neighbouring pixels (Bradski and Kaehler 2008); (3) The top hat morphology operator, within the sci-kit library, was applied to extract small elements and details from a grayscale image based on relative

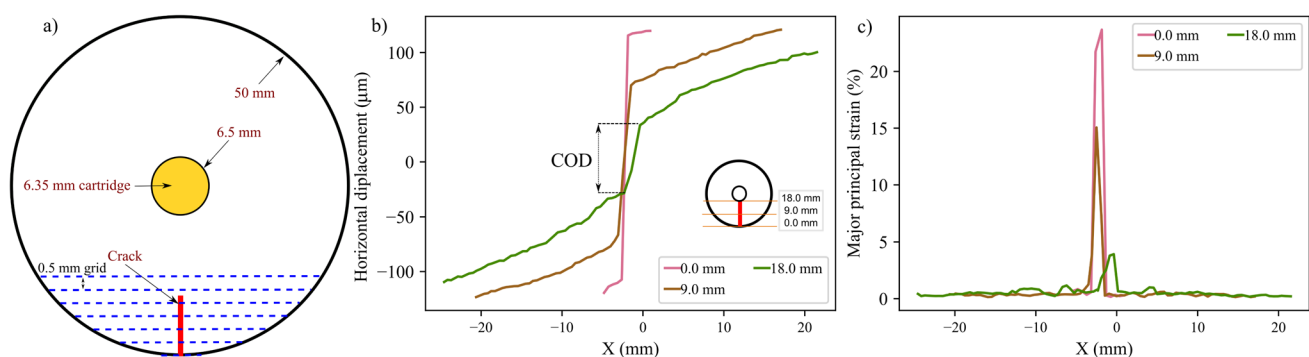


Fig. 5 a Schematic illustration of the macrocrack tracking using 0.5-mm spaced horizontal grid. b Macrocrack opening displacement (COD) determination from horizontal displacement curves. c Major principal strain plot at three different locations along the sample

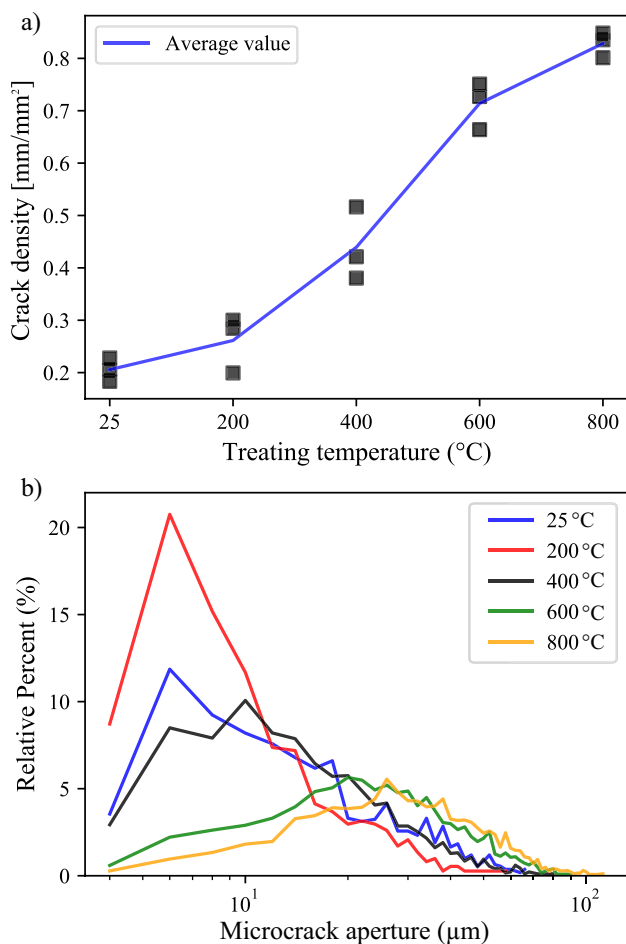


Fig. 6 **a** Evolution of thermal crack density as a function of the treating temperature and **b** microcrack aperture distribution for the different pre-treating temperatures

intensity, and to further isolate the fracture network from the background (Van der Walt et al. 2014); (4) Ridge operators were applied to detect thin fractures, using the contrast and noise level to determine the direction of the feature (Meijering et al. 2004); (5) Adaptive thresholding, a local-based thresholding technique, was adopted to correct for different intensities present in the background and threshold the image into fracture and non-fracture (background) regions.

To define discrete fractures from the thresholded image, the skeletonization algorithm was applied (Nunez-Iglesias et al. 2018). A skeleton is a single-pixel thick representation of an object, which is achieved by iteratively eroding the boundary pixels in the binary picture until only a single-pixel median representation remains, representing the effective structure of the object. The discrete fractures from the skeleton were then analysed to obtain the fracture

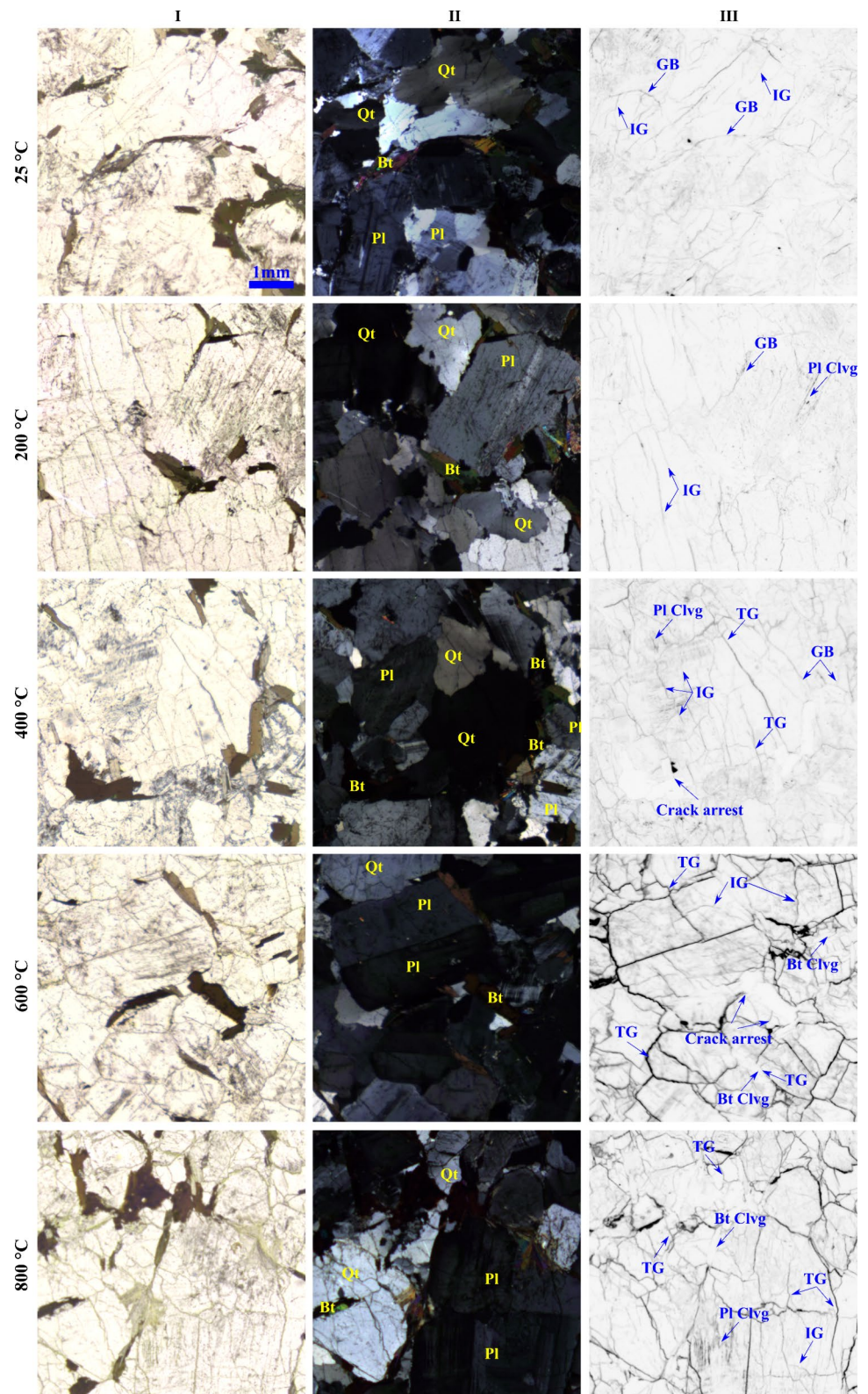
orientations, areal fracture density, and aperture for each focus area. Given the varying aperture within a single discrete fracture, a custom algorithm was developed to analyse the skeleton of each discrete fracture and measure the mean aperture of the fracture from the thin section images. To determine the aperture, a step-function was written across the length of each fracture using the known start and end coordinates, where a perpendicular line was drawn on the binary image to directly calculate the length of the aperture. For each fracture, the aperture is recorded along each point, and the average aperture is reported. The thin section image processing code was developed in Python3 (Van Rossum and Drake 2009) environment and the images were converted into numeric array objects, which allowed for a quantitative analysis to be conducted between the samples.

3.2 Cracks Identification from DIC Results

Continuum-based DIC approach implemented in GOM Correlate Pro software assumes small displacement between consecutive images. Therefore, accurate strain fields can be only obtained around cracks while the strain values across these cracks are meaningless since the strain across a crack is basically infinite (Nguyen et al. 2011). For qualitative analysis of the crack growth, major principal strain, representing tangential direction, indicates cracks propagation through strain localization, however, for quantitative analysis of the crack opening and sliding evolution displacement fields were used.

In this work, displacement jumps across crack planes were used to identify the crack and to infer its opening and sliding displacement, a process similar to those adopted in the literature (Corr et al. 2007; Dong et al. 2017; Nguyen et al. 2011). To track the spatial evolution of the macrocrack, a 0.5-mm spaced horizontal grid was used (Fig. 5a) and the variation of the displacement along these grid lines was observed. The difference between the two ends of the horizontal displacement jump at either side of the crack indicates the crack opening (Fig. 5b) and the difference of the vertical displacement between the two ends indicates its sliding. Cracks appear as peaks on the major principal strain plot (Fig. 5c). It is noteworthy that prior to the displacement and the strain fields calculations, sample images were rotated so that the macrocrack align vertically with y-direction. This way, x- and y-displacements are proxies for opening and sliding displacements of the macrocrack, respectively. Analyses were achieved using a post-processing script written in Python3 (Van Rossum and Drake 2009).

Fig. 7 I PPL, II XPL, and III FLO 6.0-mm×6.0-mm representative area for 25, 200, 400, 600, and 800 °C (*Qt* quartz, *Pl* plagioclase feldspar, *Bt* biotite, *GB* grain boundary crack (i.e., intergranular crack), *IG* intragranular crack, *TG* transgranular crack, *Clvg* crack along cleavage planes)



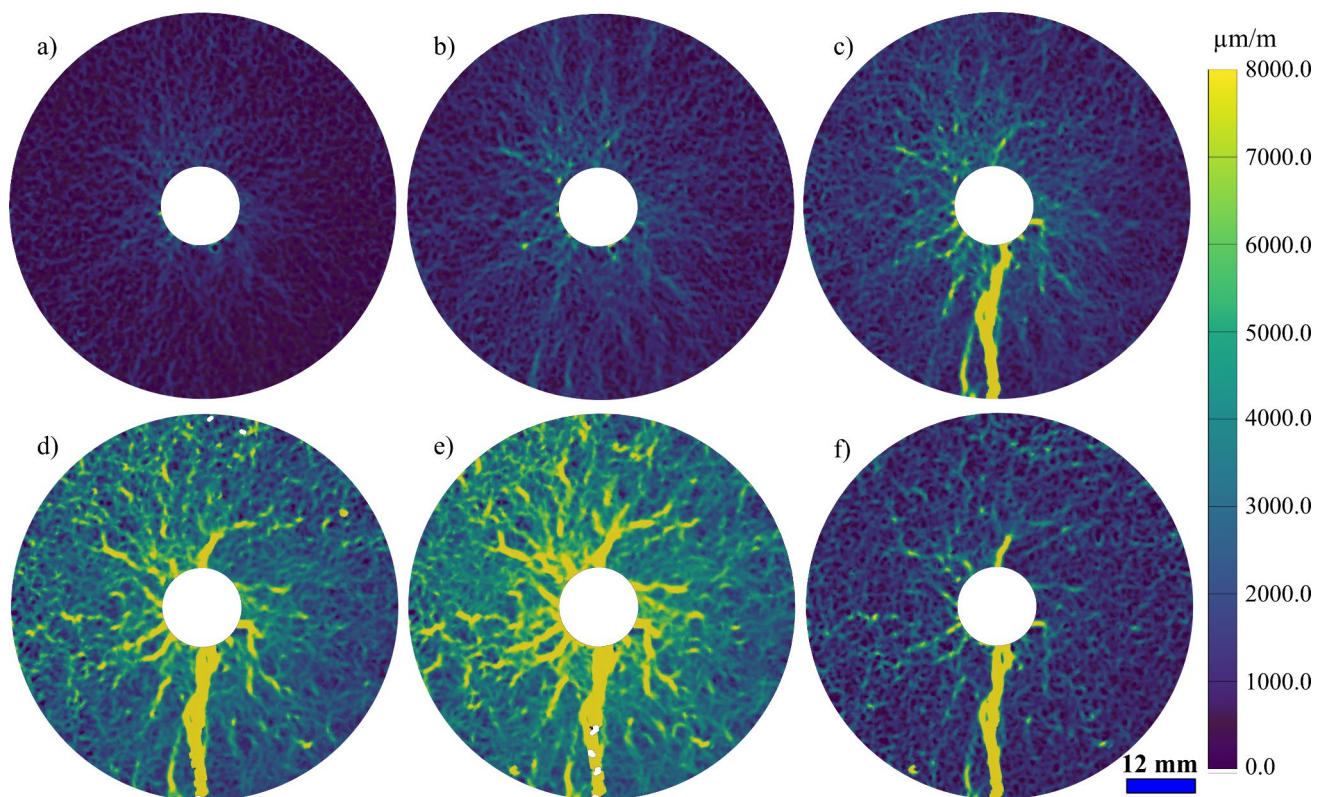


Fig. 8 Major principal strain of sample 25-S2 after **a** 100.0, **b** 200.0, **c** 300.0, **d** 800.0, **e** 1800.0 (end of heating stage), and **f** 3600.0 s (end of cooling stage). White spots in the pictures apart from the hole are missing subsets

4 Results

4.1 Microcracking Characteristics Under Thermal Pre-treatment

To observe how the treating temperature affects thermal cracking behavior of Stanstead granite, qualitative and quantitative analyses of the thin sections were performed on the Group-2 samples that were subjected to uniform thermal pre-treatment. According to the thin section analysis, Stanstead granite consists mainly of feldspar, quartz, and biotite, plus some minor amount of apatite and pyroxene. The abundance of the main minerals was $71 \pm 2\%$ feldspar, $21 \pm 2\%$ quartz, and $8 \pm 1\%$ biotite (Aboyanah et al. 2022).

Quantitatively, thermal cracking density and aperture distribution increased with the increase in the treating temperature (Fig. 6) and thermal cracking density increased drastically between 200 °C up to 600 °C, above which lower incremental increase in the cracking density was observed. Two major increases in aperture distribution were observed in the 400 and 600 °C thin sections represented by larger shift of the distribution mode towards higher aperture

values at these temperatures (Fig. 6b). Specifically, Fig. 7 shows PPL, XPL, and FLO images of one of the three 6.0-mm × 6.0-mm focus areas for each treatment temperature. Crack density in the 200 °C thin section was slightly higher than the 25 °C thin section. Biotite grains appeared to arrest some of the cracks propagating towards its grains, which is attributed to the compliant nature of biotite (Fig. 7). In the 400 °C thin section, there was a distinguishable increase in crack density and aperture (Fig. 6), mostly in the form of intergranular cracking (i.e., along grain boundaries) with few intragranular microcracks (i.e., cross-grain) in quartz and plagioclase and, to a lesser extent, along biotite cleavage planes (Fig. 7). At this temperature, most of the grain boundaries were cracked and had larger aperture than cross-grain (i.e., intragranular) cracks. Few transgranular cracks can be observed at this temperature. Cracks with the highest aperture propagated along quartz grains and those with the lowest aperture were along biotite grain boundaries. With the increased treating temperature, the length and aperture of thermal cracks increased significantly, more cracks initiated, and some coalesced into larger transgranular cracks. In the 600 °C thin section, all grain boundaries were broken,

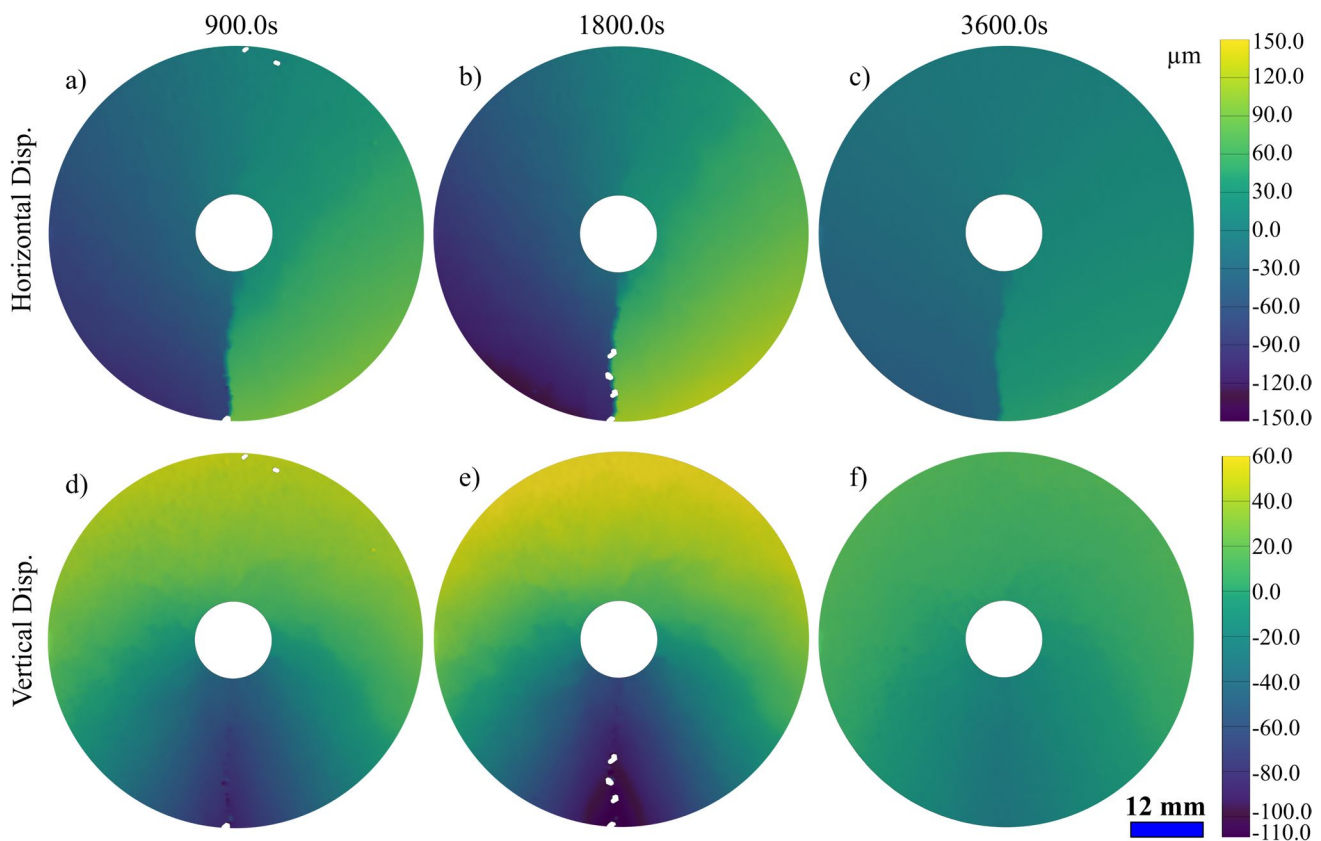


Fig. 9 Displacement field of the 25-S2 sample in the horizontal direction after **a** 900.0, **b** 1800.0 (end of heating stage), and **c** 3600.0 s (end of cooling stage) and in the vertical direction after **d** 900.0, **e**

1800.0 (end of heating stage), and **f** 3600.0 s (end of cooling stage). White spots in the pictures apart from the hole are missing subsets

formed microcrack networks, and their opening increased substantially. Meanwhile, intragranular cracking became significant specially within quartz grains. This increase in crack density and opening is associated with the quartz α - β phase transition. At 800 °C, there was a slight increase in microcrack density and aperture (Fig. 6) compared to the 600 °C, and more intragranular microcracks were noticed (Fig. 7). At this temperature, the higher apertures were associated with cracks widening across grain boundaries. At all temperatures, intragranular cracking in biotite occurred only along cleavage and transgranular cracks propagated through biotite grains only if the cleavage planes were favorably aligned, otherwise, they were arrested (Fig. 7-600III).

4.2 Thermal Cracking Evolution Under Thermal Gradient Loading

Thermal gradient loading was applied to Group-1 samples, that were uniformly thermally pre-treated to seven different temperatures, through a thermal shock by means of a

cartridge heater. Since the thermal gradient cracking pattern was typical for the samples pre-heated to the same temperature, results for sample 25-S2 are detailed in this section. It is noteworthy that the major and minor principal strain fields from the DIC represent the tangential and radial strain fields, respectively. With the cartridge turned on, the near-hole region expands due to thermal expansion as indicated by the higher positive major principal strains in the sample interior compared to the sample periphery (Fig. 8a). This near-hole expansion results in a compressive hoop stress around the hole and a tensile hoop stress in the cooler region further from the hole.

This tensile stress when in excess to the local material strength (grain-scale and grain boundaries tensile strength) nucleated cracks. Earlier in the heating stage, microcracks appeared radially scattered throughout the sample with higher spatial concentration close to the central heating source as indicated by the strain localization zones in Fig. 8b. With the temperature rise, those microcracks increased and commenced to coalesce from the sample

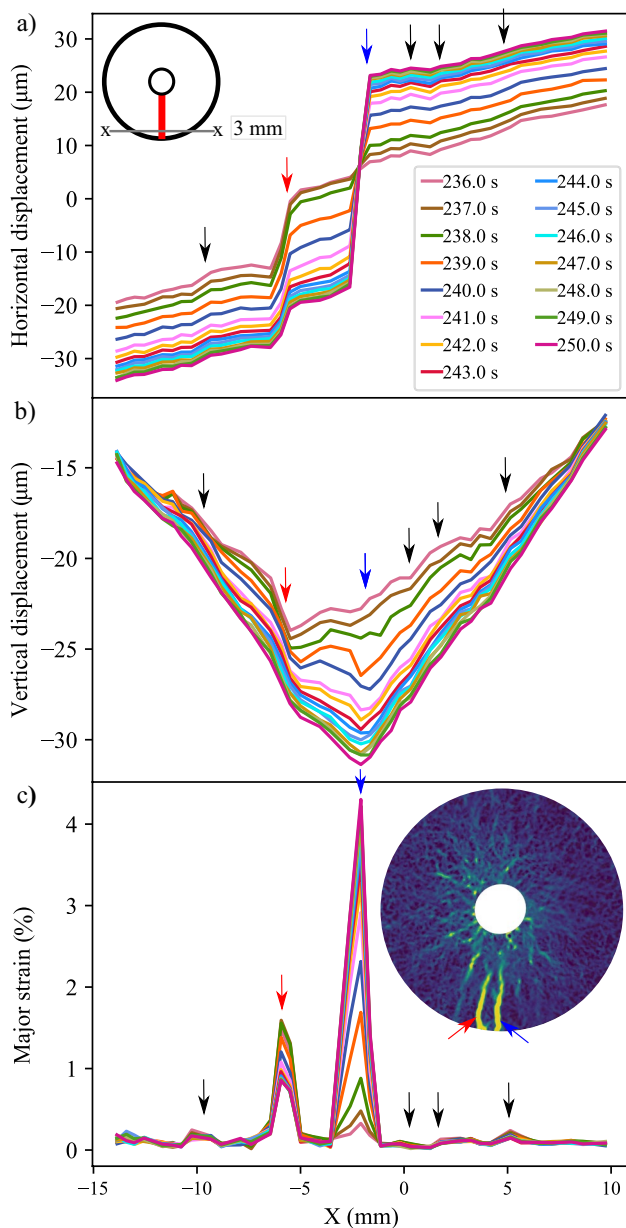


Fig. 10 Evolution of **a** horizontal displacement, **b** vertical displacement, and **c** major principal strain along 3.0-mm horizontal grid during the timesteps from 236.0 to 250.0 s for the sample 25-S2. Black arrows indicate microcracks while red and blue arrows indicate larger cracks including the propagated macrocrack (blue arrow) (**b** and **c** use the same legend as in **a**) (Colour figure online)

periphery towards the sample interior to form a macrocrack. Displacement discontinuity appears across the propagated macrocrack during the heating process (Fig. 9). It can be inferred that larger strain values occurred during the heating

stage and maximum strain was reached at the end of the heating stage (Fig. 8e).

Horizontal and vertical displacements and major principal strain evolution during the timesteps from 236.0 to 250.0 s in the heating stage at horizontal grid 3.0 mm are shown in Fig. 10 for the sample 25-S2. Cracks appear as jumps (i.e., discontinuity) on the horizontal displacement curves and as localizations on the strain curves. It is noteworthy that majority of these cracks are microcracks as indicated by the small displacement jumps (black arrows in Fig. 10). A relatively larger displacement jump, indicated by the red arrow, represents a larger crack. Another major crack is indicated by the blue arrow that resulted in the largest displacement jump. After timestep 238.0 s, this crack resulted in the reversal of the horizontal and vertical displacement curves and in the maximum strain localization, hereafter is referred to as the macrocrack (blue arrow in Fig. 10). Major principal strain at three timesteps is shown in Fig. 11 which reveals the two competing macrocracks indicated by the red and blue arrows in Fig. 10. The red-arrow crack was arrested due to the stress shadow effect from the propagated blue-arrow crack.

The opening and sliding displacements (displacement in x - and y -direction, respectively) of the subsets across the macrocrack were tracked throughout the heating and cooling stages. Earlier in the heating stage, macrocrack opening and sliding displacements were larger towards the interior of the sample due to the microcracks initiated in the higher temperature interior. With the initiation of macrocrack tip from the sample periphery with the increasing temperature, opening displacement towards the sample exterior became larger, while the sliding displacement did not exhibit a similar trend. This pattern was persistent during the cooling stage (Fig. 12). Sliding displacement was significantly lower than the opening displacement, which indicates that macrocrack coalescence was driven by mode-I cracking caused by the tensile hoop stresses. However, the nontrivial sliding of the subsets across the macrocrack does not exclude shear microcracks initiated early in the heating stage prior to the macrocrack coalescence. Macrocrack opening increased during the heating stage and reached its maximum opening at 1800.0 s (i.e., at the end of heating stage) at the sample periphery. During the cooling stage, the macrocrack closed and reached its residual opening and sliding displacements.

Crack opening across the macrocrack ends, measured at the sample periphery, exhibited different regimes with hole temperature evolution during the heating and cooling stages (Fig. 13). First, the macrocrack opening linearly increased to 4.5 μm over a temperature rise from 25 to 176 $^{\circ}\text{C}$ which suggests a period of thermoelastic deformation. With the

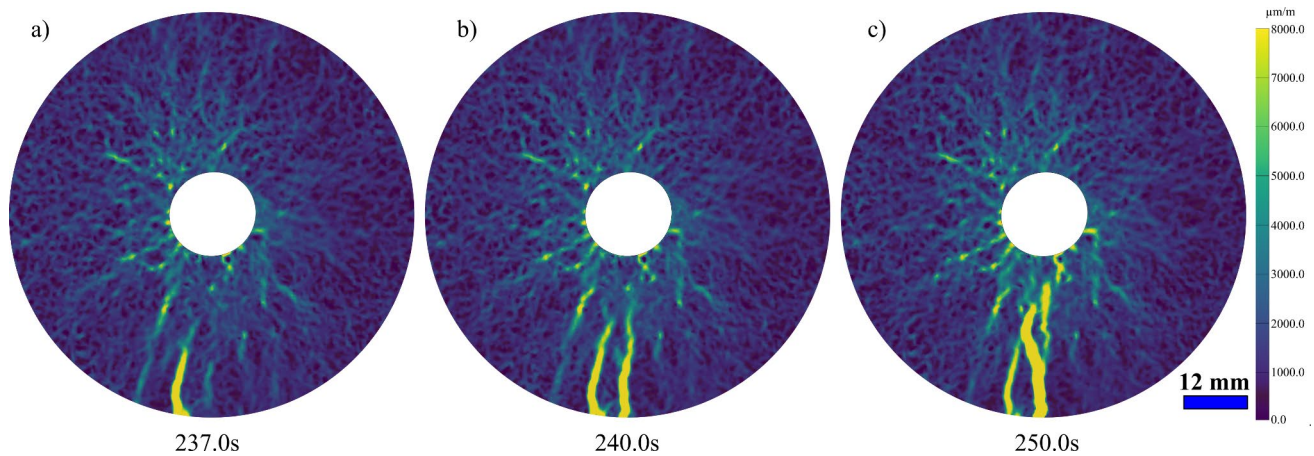


Fig. 11 Evolution of the major principal strain after **a** 237.0, **b** 240.0, and **c** 250.0 s for the sample 25-S2. At these timesteps two macrocracks were competing

temperature rise, macrocrack coalescence resulted in a dramatic jump in the opening and the onset of this jump marks the critical temperature for macrocrack coalescence, which

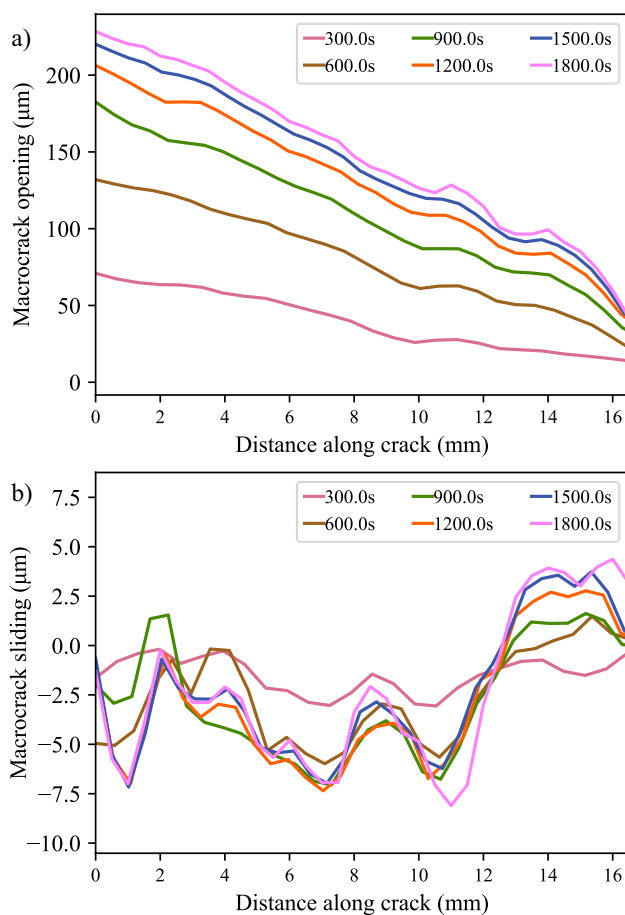


Fig. 12 **a** Opening, and **b** sliding displacements of the macrocrack interface during heating stage for the sample 25-S2

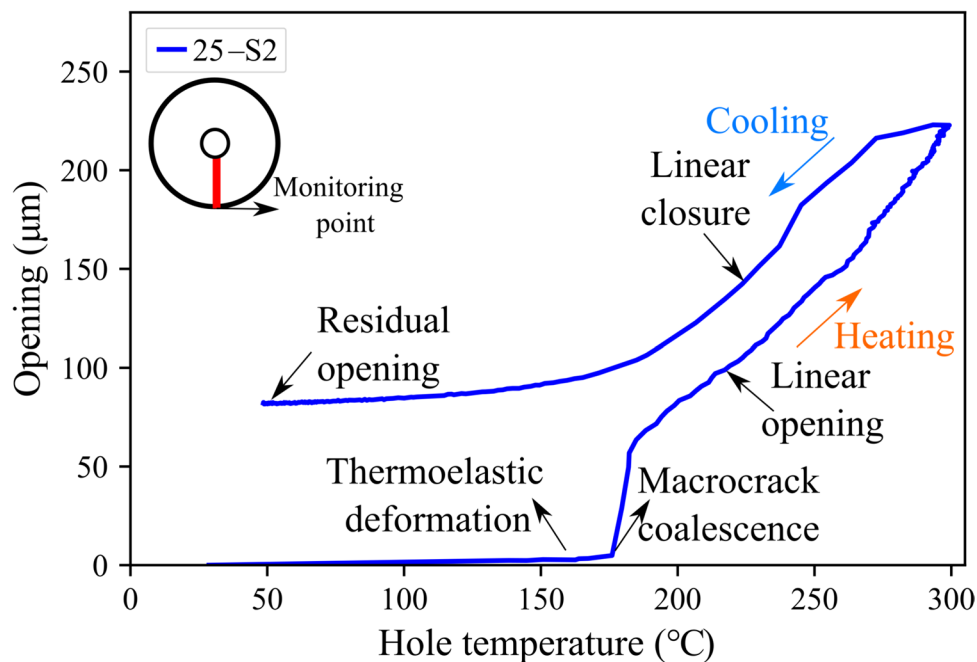
was 177 °C for sample 25-S2. Following macrocrack coalescence, a linear increase in the opening with hole temperature was observed, while in the cooling stage macrocrack closed linearly, with hole temperature decrease until the residual opening was approached.

To acquire deeper comprehension of the thermal gradient loading evolution throughout the sample, a total of twelve 4.0 mm length virtual strain gauges (VSGs) were used to track strain evolution in the 25-S2 sample at different locations shown in Fig. 14a. This gauge length was chosen to be sufficiently larger than Stanstead granite grain size (0.2–2.0 mm). Generally, all VSGs showed increasing strain trending with the temperature rise in the sample during the heating and decreasing strain to residual values during the cooling stage (Fig. 14b). By examining the VSGs results during the macrocrack propagation interval, we found that circumferential strain at the sample perimeter at three locations on the sample (VSG No. 4, 8, and 9) showed elastic strain restoration at 238.0 s when the macrocrack propagated (Fig. 14c). Such behavior indicates hoop (or tangential) stress release in the sample after macrocrack propagation. Also, VSGs perpendicular to the macrocrack (i.e., VSG No. 3 to 6) revealed instantaneous elastic strain restoration in the macrocrack perpendicular direction indicating tensile cracking behavior. The trace of the macrocrack at the sample perimeter is shown in Fig. 15.

4.3 Effect of the Pre-treatment Temperature on the Thermomechanical Behavior

Samples of Group-1 were subjected to uniform thermal pre-treatment to various target temperatures, followed by typical thermal gradient loading. Results revealed that the pre-treatment and the consequent thermal cracking density and aperture significantly influenced the thermomechanical

Fig. 13 Crack opening evolution with hole temperature for sample 25-S2



response to the thermal gradient loading. As shown in Figs. 16, 17 and 18, all the samples pre-treated at 25, 200, 300, and 400 °C underwent macroscopic cracking, which was absent in all the samples pre-treated at 600 and 800 °C. Sample 400-S1 had two macrocracks although they have smaller opening and only one of the samples pre-treated at 500 °C, namely 500-S2, had a macroscopic crack. Qualitatively, more periphery cracks were observed in the 500-S1 and 500-S3, as well as in all samples treated to 600 and 800 °C, compared to those pre-treated at lower temperatures (Fig. 19). These cracks initiated early on during the heating stage before being arrested and have lower opening compared with the extended macrocracks. Moreover, more cracks were noticeable in a radial pattern in the hotter region near the hole in the samples pre-treated at temperatures up to 400 °C than in those treated at higher temperatures (Fig. 19). The traces of these near-hole cracks appeared at the end of the cooling stage in the samples pre-treated at 400 °C or lower (Fig. 17). It is noteworthy that all the samples that underwent macroscopic cracking had a single macrocrack except for 400-S1, which had two macrocracks with smaller openings. This behavior can be attributed to initial defects implied by the granite samples heterogeneity. These defects represented the least-resistance path that coalesced to a single macrocrack under the applied thermal gradient loading. Moreover, the macrocracking of the samples occurred during the heating stage, not the cooling stage. Major principal strain relative distribution at the end of the heating stage

showed a general trend towards lower strain values as the uniform thermal pre-treating temperature increased which indicated, for linear elastic brittle material, lower tensile stresses build-up in the samples pre-treated at higher temperatures (Fig. 20).

Quantitative analysis of samples with macroscopic cracking, revealed that the macrocrack opening linearly increased from the sample hole to the periphery during both heating and cooling stages (Fig. 21). Also, thermal gradient macrocrack coalescence temperature (i.e., critical temperature) increased with increasing pre-treating temperature, while the maximum macrocrack opening at the sample periphery (at the end of the heating stage) showed an opposite trend (Fig. 22). Coalescence temperature and opening displacement showed similar trend with the pre-existing crack density inferred from thin sections analysis of Group-2 samples. Evolution of macrocrack opening at the sample periphery for five different samples is illustrated in Fig. 23. It can be noticed that coalescence temperature increased with the pre-treatment temperature and interestingly the opening rate to the maximum opening increased as reflected by the slope of the heating curve after macrocrack coalescence.

Moreover, strain fields acquired by DIC demonstrated microcrack closure signature during the heating stage in the samples pre-treated at 600 and 800 °C which have higher initial crack density and aperture distribution. Minor principal strain, which represents radial strain field, showed crack closure signature in the radial direction (Fig. 24a) where

Fig. 14 **a** Virtual strain gauges (VSGs) on the 25-S2 sample. **b** Strain evolution during the test measured by the VSGs in **a**. **c** Strain response during the macrocrack propagation interval. The dashed line in **c** indicates macrocrack coalescence timestep

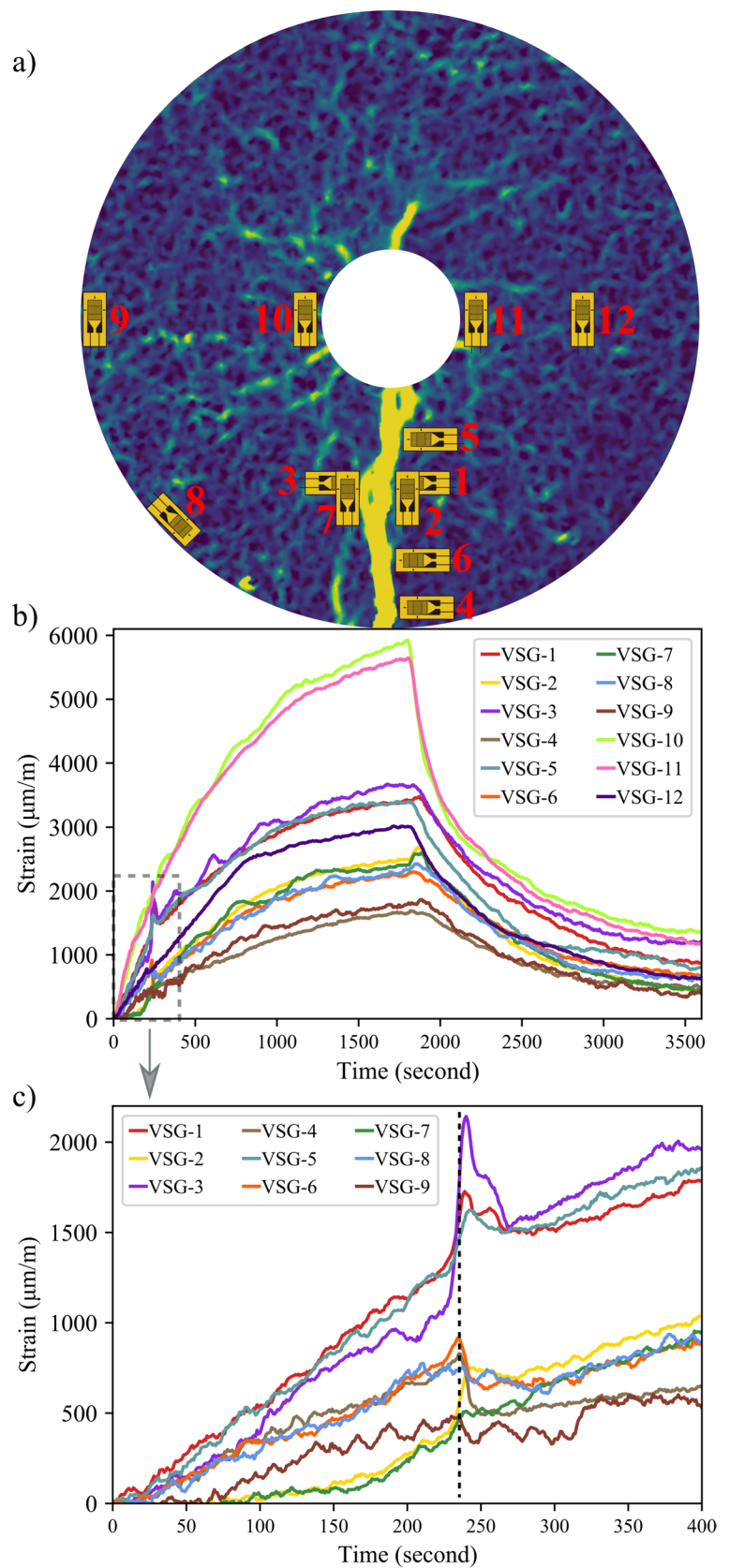


Fig. 15 Macrocrack trace, between the two red lines, at the circumferential surface of sample 25-S2 (Colour figure online)



the stresses perpendicular to these closure locations were compressive (Aboyanah et al. 2023), whereas major principal strain, which represents tangential strain field, demonstrated crack closure zones in the tangential direction, which appeared to result from stress shadowing adjacent to initiated microcracks (Fig. 24b), where the stresses are tensile (Aboyanah et al. 2023). The count of subsets with large negative (i.e., contraction or shortening) major principal strain increased in the early heating stage (Fig. 24c), which indicated crack closure during the expansion of the mineral grains. It is noteworthy that the strain fields in Fig. 24 were analyzed using a step size of 5 pixels to acquire higher strain resolution.

5 Discussion

5.1 Thermomechanical Behavior During Uniform and Thermal Gradient Heating

This paper provides quantitative and qualitative insights on the effect of thermal pre-treatment and the consequent cracking density and aperture on the thermomechanical response of granitic rocks under thermal gradient loading. The thermal cracking mechanism under uniform heating is attributed to the differential or uneven thermal expansion of the rock constituting minerals, as uniform spatial distribution of microcracks seen in the thin sections. With increased treating temperature, thermal cracking density increased. The thermal cracking pattern showed that intergranular cracking was the prevailing cracking pattern and intragranular cracks exist and their proportion increased with increasing temperature above 400 °C. Also, we started to observe significant increase in the thermal cracks density and aperture in the samples treated at 400 °C, which

was attributed to the displacive phase transition in feldspar minerals between 200 and 300 °C (Li et al. 2021b; Liu et al. 2018; Mo et al. 2022) and the decrepitated bound, crystal, and structural water between 200 and 400 °C, which resulted in further microcracking (Sun et al. 2015; Wang et al. 1989; Yang et al. 2017; Zhang et al. 2016). Tian et al. (2020) reported an increase in the permeability of granite at temperatures higher than 300 °C due to microcracking. The microcracks density and aperture further increased at 600 °C due to the α - β phase transition in quartz which occurs at 573 °C at atmospheric pressure (Nasseri et al. 2007) and chemical changes in the granite constituting minerals such as siderite, magnetite, pyrrhotite, pyrite, illite, and kaolinite between 500 and 600 °C (Just and Kontny 2012).

Thermal gradient loading that followed the low heating rate uniform thermal pre-treatment then further cracked the rock. Real-time DIC observations revealed that the failure mechanism in this stage is dominated by the thermal gradient stresses, where the microcracks initiated around the heating source and spread outwards followed by macrocrack coalescence from sample periphery driven by the expansion of the hotter interior of the sample which exerted tensile stresses on the cooler exterior. This contradicts Jansen et al. (1993) conclusion, which suggested that thermal gradient macrocracking initiates from the free sample periphery and propagates inward toward the heating source. Moreover, although the macrocrack coalescence was driven by tensile hoop stress buildup, the initiated microcracks along the macrocrack had nontrivial sliding displacement which indicate shear cracking mode. Jansen et al. (1993) documented the dominance of shear microcracking during thermal gradient loading using AE monitoring. However, Zhao (2016) and Xia et al. (2014), using numerical simulation of the thermal gradient loading, observed tensile microcracking dominance. DIC results also revealed higher cracking density in the hotter interior of the sample around the heating hole, which was hypothesized by Jansen et al. (1993) but was not captured by their AE system. These interior cracks were the result of both thermal gradient and differential thermal expansion mechanisms in the hotter interior. Another intriguing finding was that samples pre-treated at temperatures up to 400 °C (i.e., low initial crack density) experienced macroscopic cracking, while those pre-treated at higher temperatures (i.e., higher initial crack density) did not exhibit the formation of any visible macrocracks, although, they had multiple periphery cracks (opening of these cracks did not exceed 30 μ m at the end of the heating stage) nucleated early during the heating stage (Fig. 16). These cracks under elevated hole temperature propagated stably and arrested somewhere

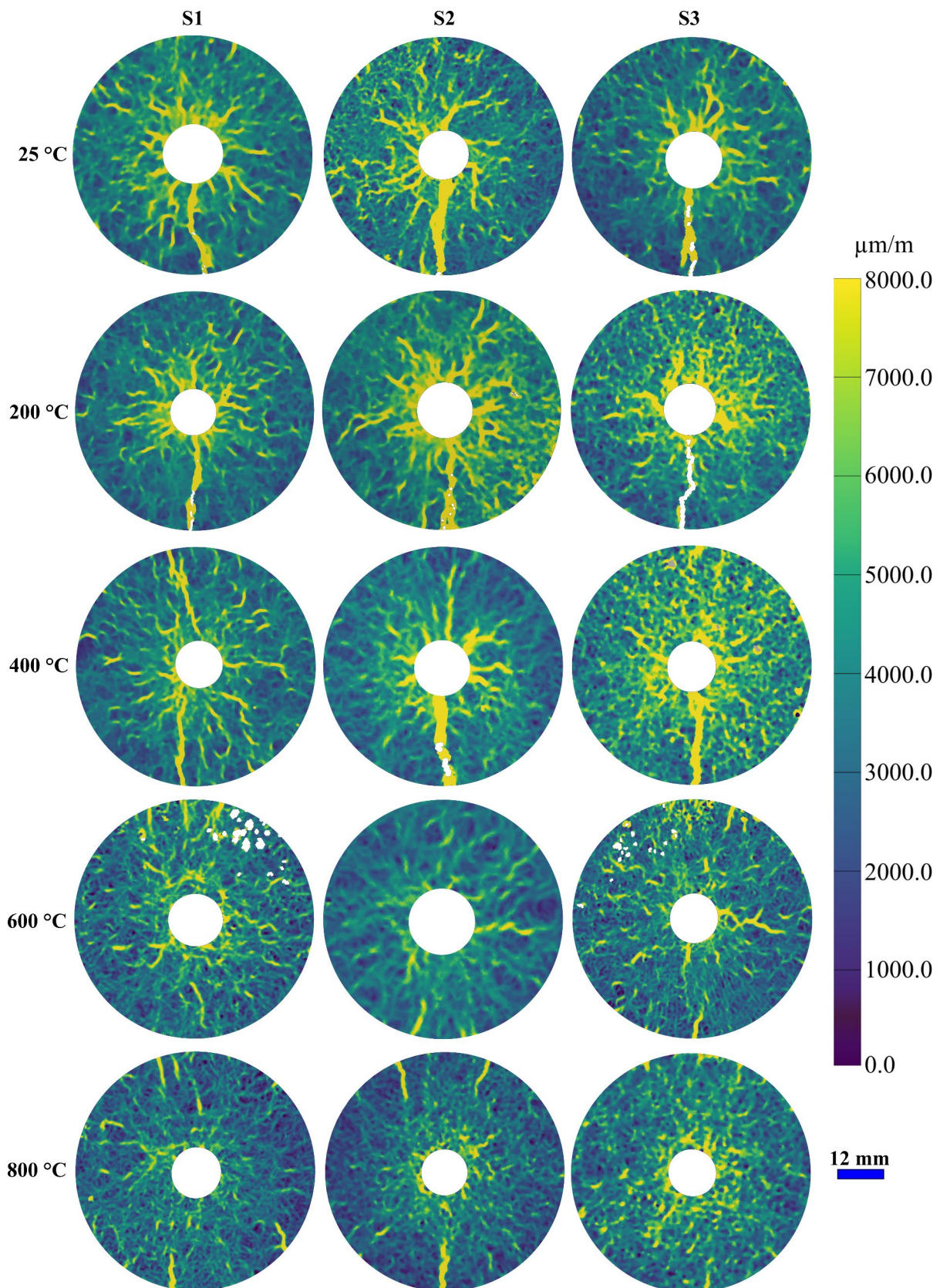


Fig. 16 Major principal strain at the end of the heating stage (i.e., 1800.0 s). Samples pre-treated at 25, 200, 400 °C underwent macroscopic cracking shown as high-strain zone. White spots in the pictures apart from the hole are missing subsets

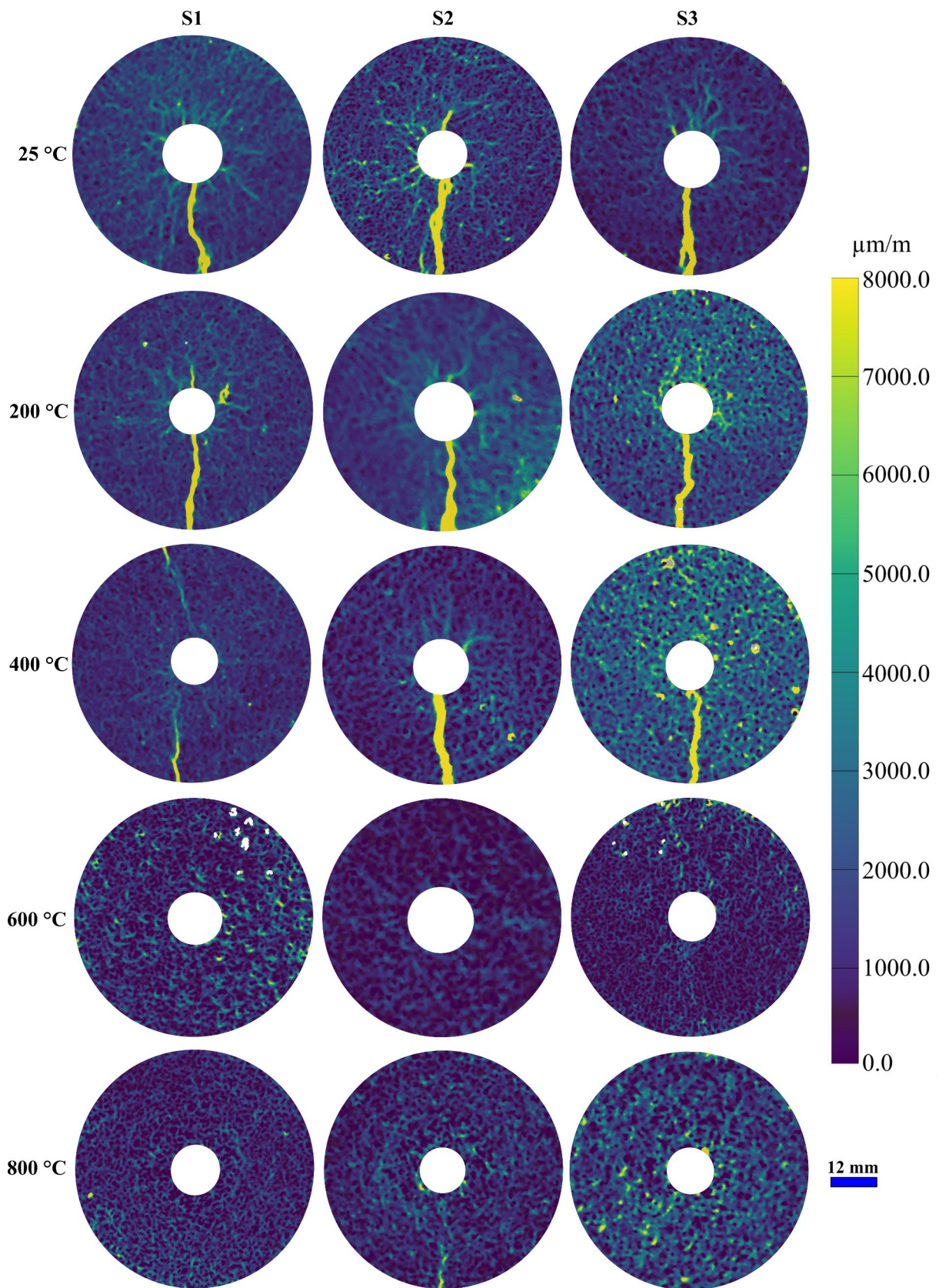


Fig. 17 Major principal strain at the end of the cooling stage (i.e., 3600.0 s). Samples pre-treated at 25, 200, 400 °C underwent macroscopic cracking shown as high-strain zone. White spots in the pictures apart from the hole are missing subsets

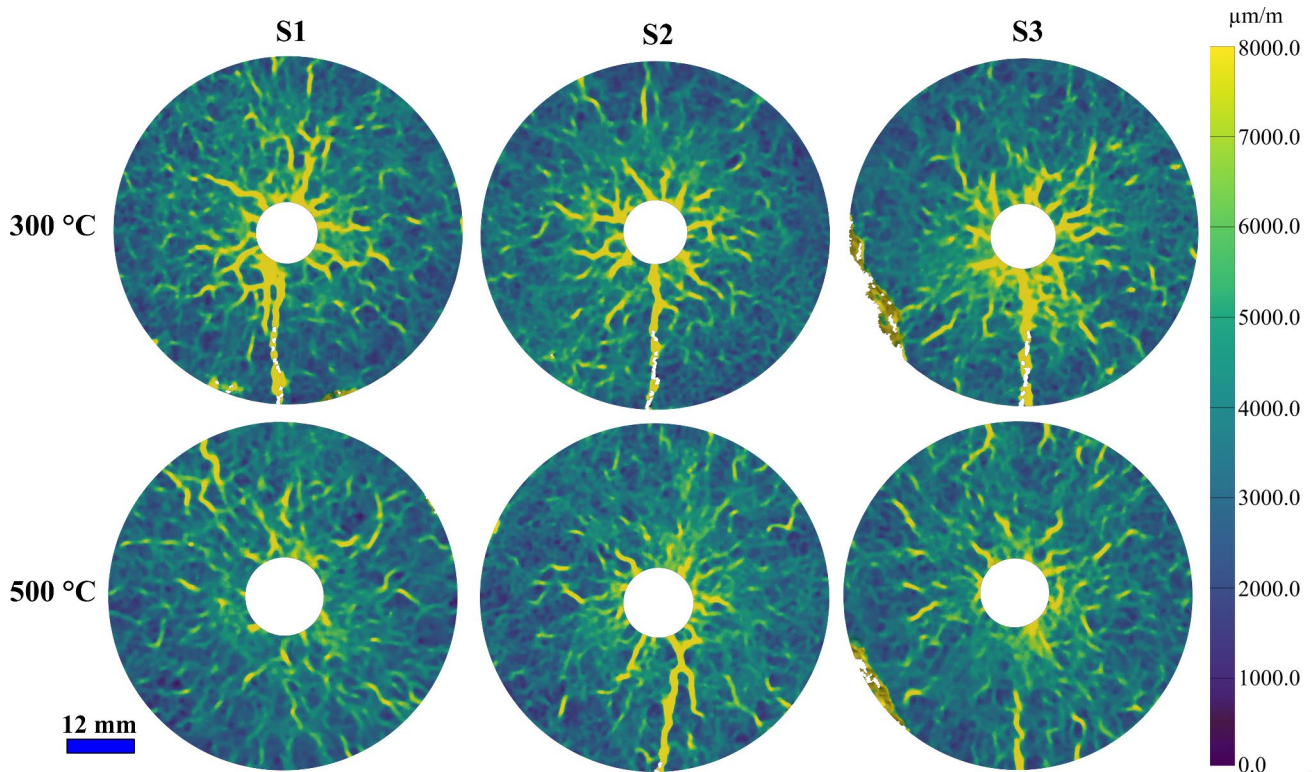


Fig. 18 Major principal strain at the end of the heating stage (i.e., 1800.0 s) for samples pre-heated at 300 and 500 °C. White spots in the pictures apart from the hole are missing subsets

between the hole and the sample periphery. The lack of macroscopic cracks in the samples pre-treated at temperatures over 400 °C was explained as due to the high microcrack density and aperture, which accommodated the thermal expansion of the mineral grains during the thermal gradient loading (Aboyanah et al. 2022; Cooper and Simmons 1977; Fredrich and Wong 1986; Yang et al. 2017), resulting in delayed and reduced tensile hoop stress build-up. The expansion-accommodating behavior was captured during the heating stage as microcracks closure in both the tangential and radial directions in our tests (Fig. 24). Pre-existing crack closure occurred as a result of stress shadowing from the initiated new cracks, the opening of pre-existing ones, or mineral grains expansion (Fig. 24). Moreover, the multiple periphery cracks in these samples can be explained by the dual effect of the abundant initial microcracks in the samples pre-treated at higher temperatures (over 400 °C). Favorably oriented periphery microcracks facilitated the coalescence of the thermal gradient crack at the sample periphery before it got arrested by unfavorably oriented microcracks through

the blunting effect (Aboyanah et al. 2022; Alm et al. 1985; Balme et al. 2004; Meredith and Atkinson 1985). Moreover, DIC data revealed that samples pre-treated to temperature between 300 and 500 °C underwent macroscopic crack coalescence at lower temperatures that ranged from 220 to 260 °C (Fig. 22). Therefore, thermomechanical behavior of the samples did not exhibit temperature memory, commonly referred to as Kaiser effect (Griffiths et al. 2018), during thermal gradient loading. The different type of the thermal loading adopted in our staged heating (i.e., uniform heating followed by thermal gradient heating) might be contributing to this behavior.

The varying macrocrack coalescence temperature also strongly suggested the existence of a thermomechanical transition zone in granites, well below α - β quartz phase transition at 573 °C, that depends on the initial crack density and aperture, and grains thermal and mechanical properties. We observed this transition zone between 300 and 500 °C in which all samples pre-treated at lower temperatures underwent macroscopic cracking, while all those pre-treated at

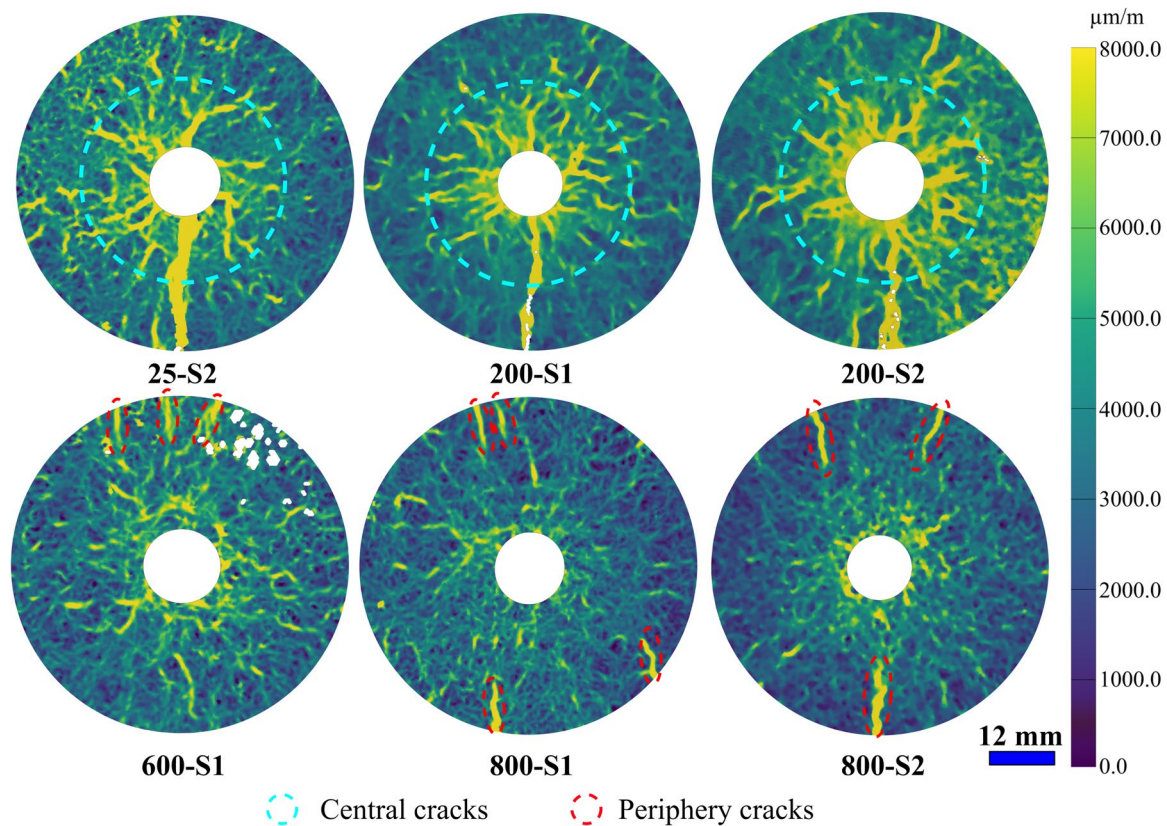


Fig. 19 Central and periphery cracks, highlighted in cyan and red ovals, respectively, showed on major principal strain at the end of the heating stage (i.e., 1800.0 s) for selected samples. White spots in the pictures apart from the hole are missing subsets

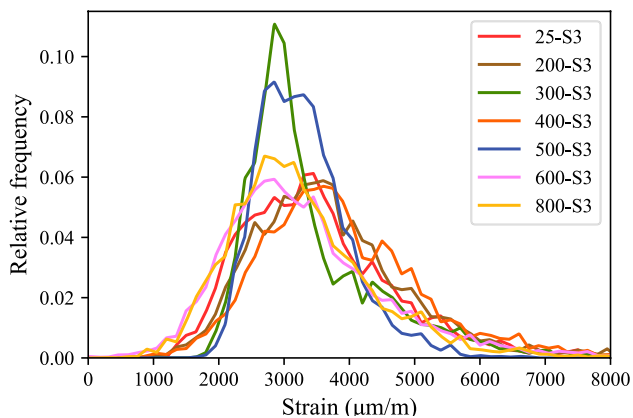


Fig. 20 Major principal strain distribution at the end of the heating stage (i.e., 1800.0 s) for selected samples pre-treated at seven different temperatures

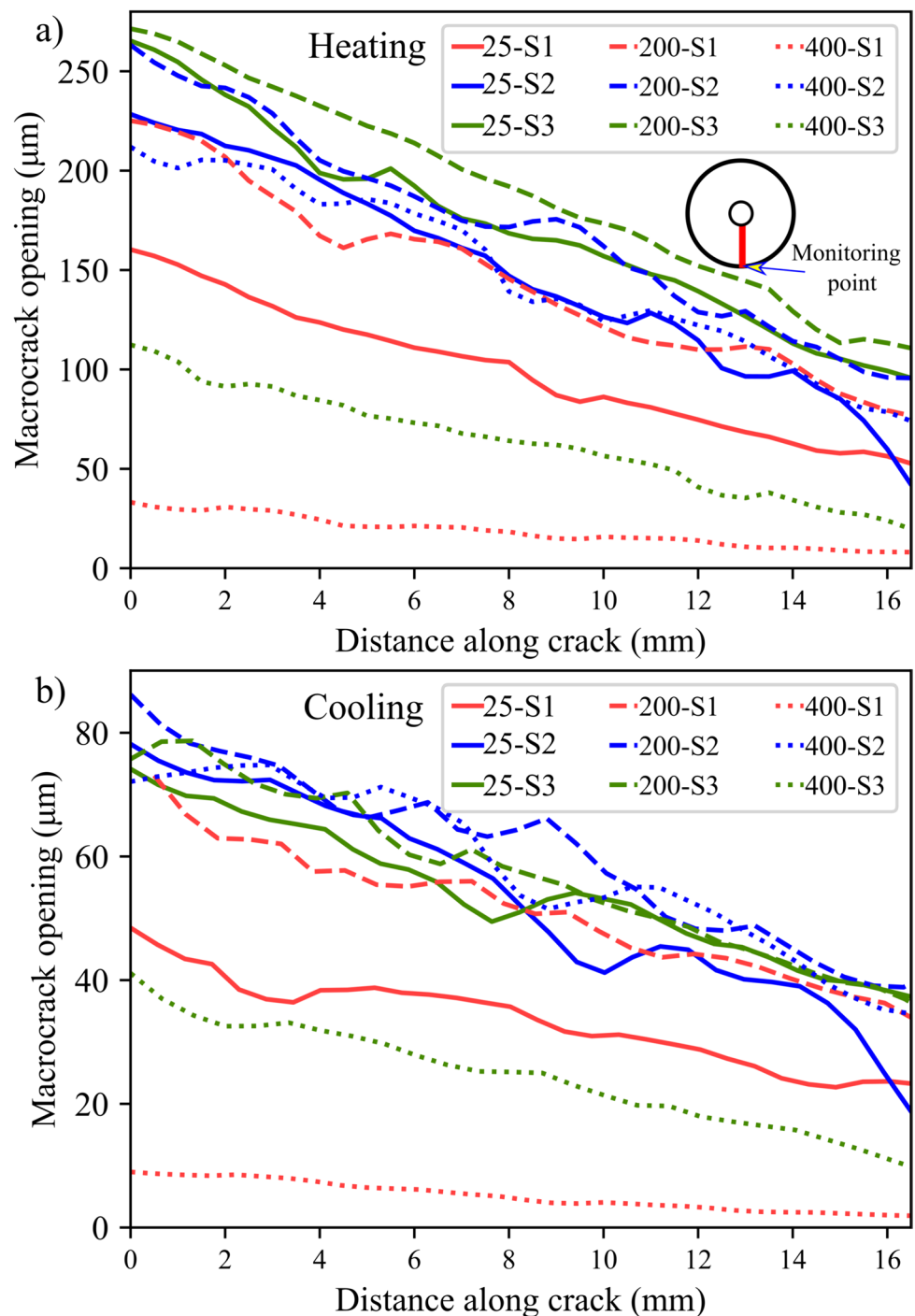
higher temperatures did not macroscopically crack. This observation was supported by the significant increase in crack count and aperture in the 400 °C thin section (Fig. 6). Moreover, DIC analysis revealed that thermal cracking in

granite mainly occurred during heating rather than cooling, in contradiction with the thermomechanical behavior of some volcanic rocks (Browning et al. 2016; Heap et al. 2014) and porcelain (Kirchhoff et al. 1982) undergoing more thermal cracking during cooling. Heating-dominated thermal cracking in granite has also been observed using AE monitoring (Griffiths et al. 2018).

5.2 Research Impact

Alterations in the Earth crust's in situ temperature field induce thermal stresses, potentially leading to thermal cracking (Gunatilake 2023; Johnson et al. 2021; Rowland and Simmons 2012; Sun et al. 2023; Veloso et al. 2020). Notably, thermal gradient stresses within the Earth's crust can rejuvenate hydrothermal circulation through grain-scale cracks (Olive and Crone 2018) and elucidate plate tectonic convection through kilometeric-scale cracks (Korenaga 2007). Additionally, utilizing thermal treatments on rocks has proven effective for hard rock breakage, widely applied in geotechnical engineering, enhanced oil recovery, geothermal energy exploitation, mining, and tunnel excavation (Chen et al. 2021; Cui et al. 2020; Kafashi et al. 2023; Lin et al. 2023; Liu et al. 2023; Taheri-Shakib and Kantzas

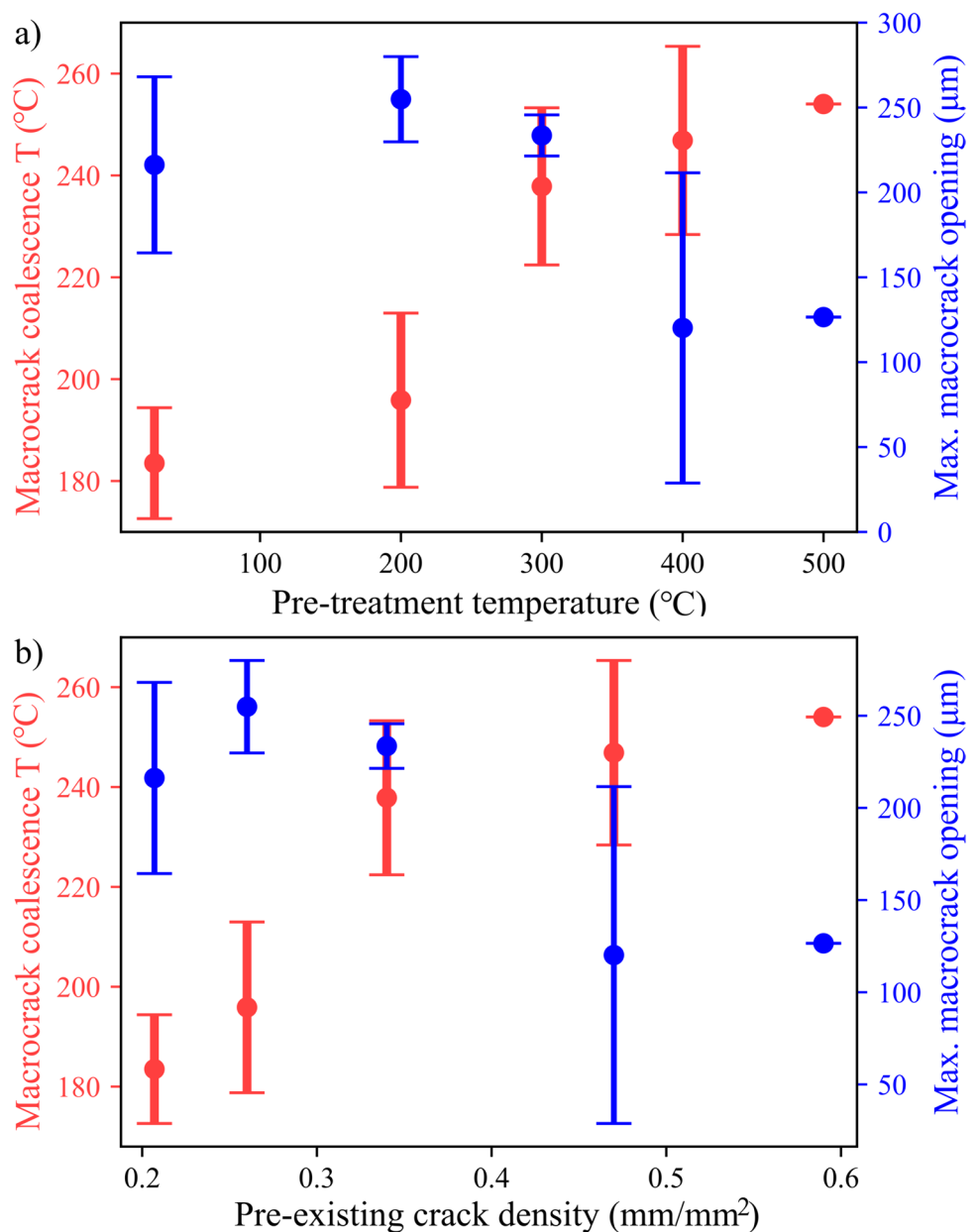
Fig. 21 Macrocrack opening along the crack length for the samples treated at 25, 200, and 400 °C which underwent macroscopic cracking at **a** the end of the heating stage, i.e., 1800.0 s, and **b** the end of the cooling stage, i.e., 3600.0 s



2021) (Fig. 25). The thermal uniform pre-treatment temperature range (25–800 °C) covered in this paper is comparable to thermal loading in oil/gas reservoir or underground nuclear storage applications in the vicinity of the heating source. For instance, high-power laser application in drilling and perforating oil and gas reservoirs can elevate rock temperatures beyond 1200 °C (Batarseh et al. 2003, 2021;

Han et al. 2019; Xu et al. 2024), whereas lower temperatures (< 150 °C) are encountered in the vicinity of decaying nuclear waste (Buscheck et al. 2002; Cho et al. 2012; Lisjak et al. 2023). Moreover, as one moves away from the heat source towards in situ temperatures, the thermal gradient cracking mechanism becomes more pronounced.

Fig. 22 **a** Evolution of macrocrack coalescence temperature and opening at the sample periphery with **a** pre-treatment temperature and **b** pre-existing crack density. Bars indicate minimum, average, and maximum values. No macrocracks exist in the samples pre-treated at 600 and 800 °C



The staged heating treatment presented in this paper, considering crack density and aperture, proposed an approach that adequately reflects the situation for many underground engineering applications with varying in-situ damage intensity in rocks undergoing heating treatment. In geothermal systems, for instance, the heating induced from magma migration and the cooling effect of the circulated water and the heating effect from the surrounding hot rock induce thermal gradient loading in the reservoir rock (Olive and Crone 2018; Xue et al. 2023). The newly generated cracks due to the induced thermal gradients will be dependent on the initial crack density and aperture inherited from the in-situ thermal and confining pressure history. Thermal gradient induced cracking appeared in radial pattern around the

heating source in our experiments, therefore, preferential cracks orientation from well imaging can be used as an indicator of high thermal loading in the layers overlying magma chambers during the drilling for supercritical geothermal resources at relatively shallow depths (Scott et al. 2015) to avoid drilling into the magma and losing costly drilling equipment.

Moreover, in the cyclic heating process, it is observed that the mechanical properties (e.g., uniaxial compressive strength and Young's modulus) of rock samples deteriorate with the heating cycles, however, the deterioration rate may decrease, and the properties may remain unchanged after a certain number of cycles (Yu et al. 2020). This phenomenon is similar to that observed in our experiments from

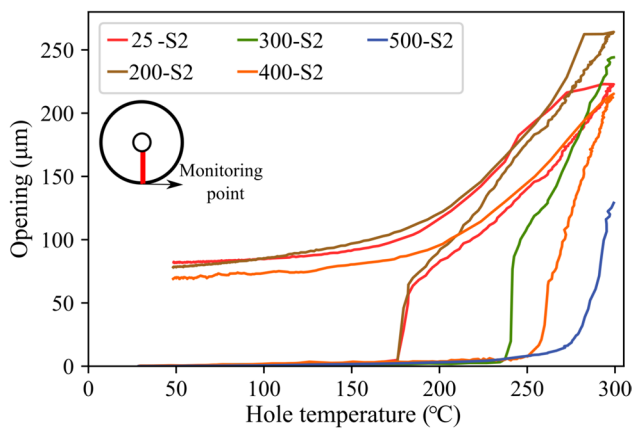


Fig. 23 Evolution of macrocrack opening displacement at the sample periphery for five different samples pre-treated at different temperatures. Test for the 300-S2 and 500-S2 samples was terminated at the end of the heating stage

microcracking perspective where the newly generated cracks induced by thermal gradient might get arrested by the existing microcracks generated from the uniform heating pre-treatment. To a more general context, the cracks here are not only the thermally induced cracks but can also be pre-existing cracks during tectonic process or confining stresses.

On a different front, previous research on thermal gradient cracking has adopted thermally untreated samples with negligible pre-existing crack density (Carlson et al. 1993; Jansen et al. 1993) that was used to calibrate initially intact numerical samples (Wanne and Young 2008; Xia et al. 2014; Zhao 2016). However, rocks are heterogeneous materials containing microcracks, their mechanical and thermomechanical behavior depend significantly on the density and concentration of these microcracks. Therefore, the sample intactness assumption of the synthetic models limits their ability to investigate the role of pre-existing fractures and defects in thermal cracking evolution. The present fundamental research is crucial for calibrating numerical models to incorporate pre-existing microcracks and porosity variations instead of the widely adopted assumption of initially intact numerical rock samples (Aboyanah et al. 2021; Wang and Konietzky 2019, 2022; Wanne and Young 2008; Xia et al. 2014; Zhao 2016). This will promote realistic simulation of various in situ high-pressure and high-temperature underground scenarios that entail initially fractured rock masses.

6 Conclusions

In this work, we designed a staged heating experiment to investigate thermal gradient loading response to thermal pre-treatment and the consequent crack density and aperture. We

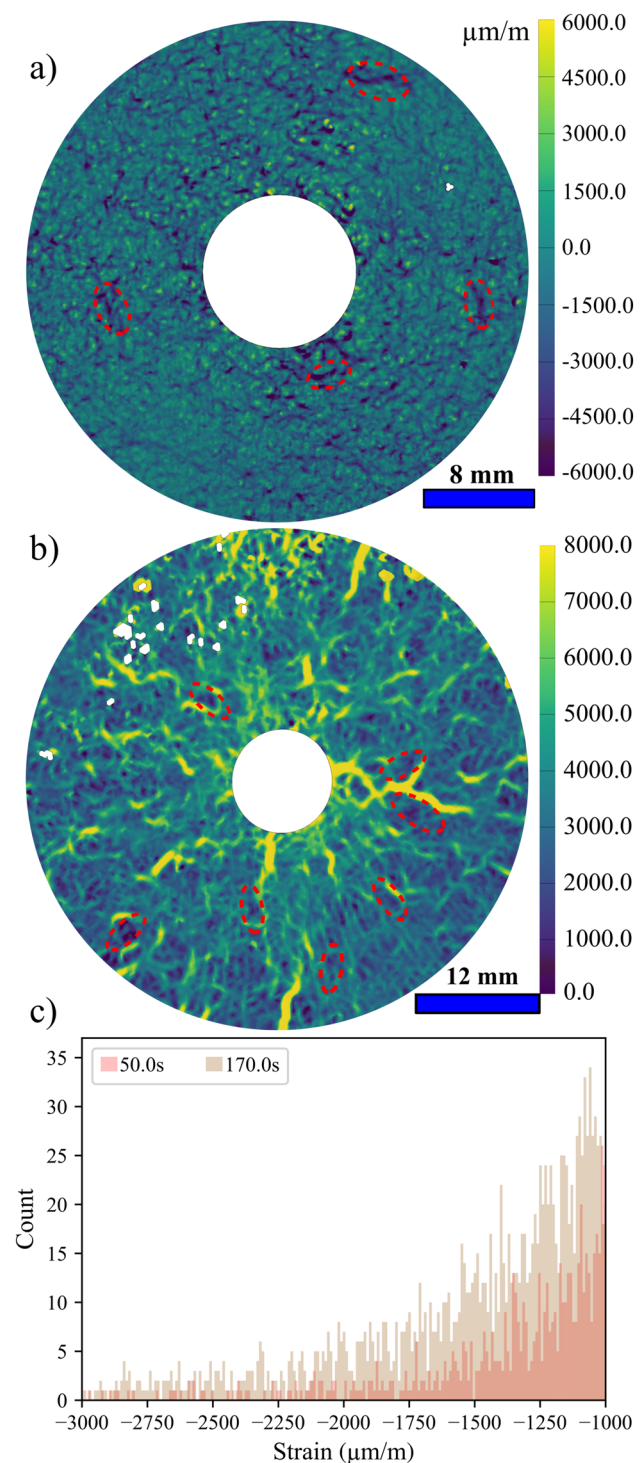
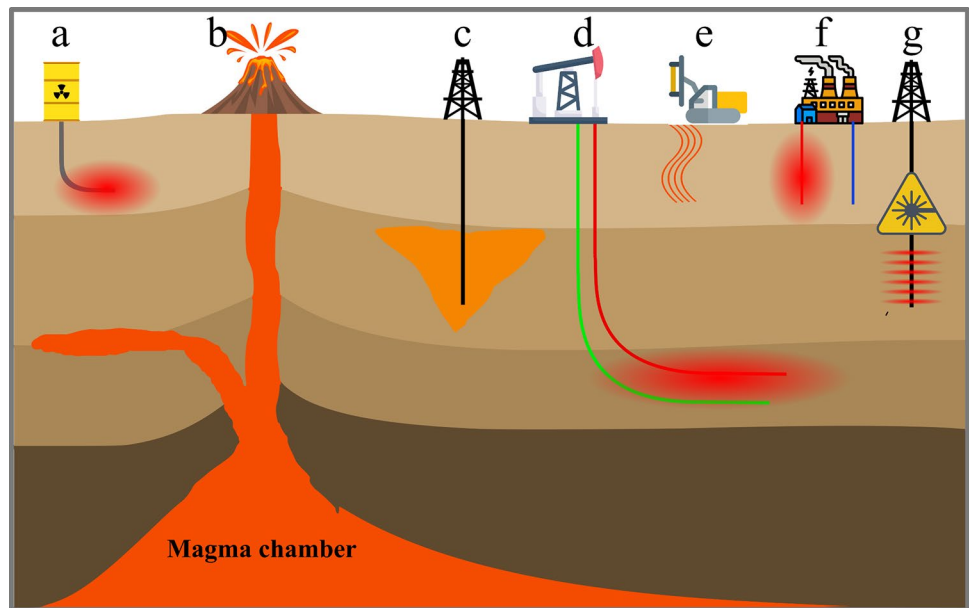


Fig. 24 **a** Minor principal (radial) strain field after 250.0 s into the heating stage for sample 800-S1. **b** Major principal (tangential) strain field at the end of the heating stage for sample 600-S3. Some cracks closure spots are encircled in red. White spots in the pictures apart from the hole are missing subsets. **c** Increase in the negative major principal strain count from timestep 50.0 s to 170.0 s indicating crack closure early during the heating stage

Fig. 25 Underground activities entailing thermal gradient loading: **a** underground nuclear waste repositories, **b** volcanic activity and magma migration, **c** in situ oil combustion enhanced heavy oil recovery, **d** steam-assisted gravity drainage (SAGD) operation, **e** microwave-assisted drilling, **f** seasonal underground heat storage, and **g** laser perforation



adopted petrographic analysis of thin section images and digital image correlation (DIC) to conduct comprehensive quantitative and qualitative analysis. The conclusions from our findings are as follows:

1. Uniform thermal pre-treatment revealed that thermal cracking density increased with increased treating temperature. Significant increase in thermal cracks aperture was observed in the samples treated at 400 °C and the cracks aperture further increased at 600 °C, which can be attributed to the feldspar displacive phase transition and the escape of bound, crystal, and structural water between 200 and 400 °C and the quartz α - β phase transition around 573 °C. Also, intergranular cracking was the prevailing cracking pattern and almost all grain boundaries were cracked at 600 °C. Above 400 °C, intragranular cracks increased with increasing temperature. Moreover, intragranular cracking in biotite grains occurred along cleavage planes and transgranular cracking propagated through biotite only if the cleavage planes were favorably oriented.
2. DIC results revealed that during thermal gradient loading microcracks nucleated close to the heating source in radial pattern while the macrocrack coalescence commenced from the free sample periphery. With temperature rise, the macrocrack propagated inward towards the heating hole through the coalescence of microcracks.
3. Thermal gradient macrocrack opening increased linearly with the temperature during the heating process, with the largest opening located at the sample perimeter, decreasing linearly to the lowest value at the hole. During the cooling stage, opening decreased linearly with temperature drop due to the cooling-induced shrinkage
4. Samples pre-treated at 600 and 800 °C with higher pre-existing crack density and aperture did not experience macrocracking and were less sensitive to the thermal gradient loading compared with the samples pre-treated at lower temperatures. This behavior is attributed to the effect of the abundant microcracks in the samples allowing free mineral grains expansion which was captured using DIC. Thermal gradient macrocrack coalescence temperature increased with the increased pre-treating temperature and the pre-existing crack density. Moreover, a transition zone from 300 to 500 °C appeared to affect the thermomechanical behavior of granitic rocks in response to the thermal shock.

Acknowledgements This work has been supported through the Natural Sciences and Engineering Research Council of Canada (NSERC) Discovery Grants 341275, NSERC/Energi Simulation Industrial Research Chair program, and State Key Laboratory of Geohazard Prevention and Geoenvironment Protection Open Fund (Grant No. SKLGP2024K001).

Author Contributions KRA: conceptualization, methodology, investigation, formal analysis, visualization, thin sections preparation, writing—original draft; EO: thin sections preparation and quantification, visualization, writing—review and editing; AA: methodology, writing—review and editing; LS: methodology, writing—review and editing; KP: thin sections preparation and quantification, supervision, writing—review and editing; GG: supervision, writing—review and editing, funding acquisition.

Funding This work has been supported through the Natural Sciences and Engineering Research Council of Canada (NSERC) Discovery

Grants 341275, NSERC/Energi Simulation Industrial Research Chair program, and State Key Laboratory of Geohazard Prevention and Geoenvironment Protection Open Fund (Grant No. SKLGP2024K001).

Data availability Data available on request from the authors.

Declarations

Conflict of Interest The authors declare that they have no known competing financial interests or personal relationships that could have appeared to influence the work reported in this paper.

References

- Abdelaziz A, Aboyanah KR, Adams M, Grasselli G (2023) Mechanical characterization, anisotropy, and failure pattern of unconventional reservoirs for wellbore stability and fracture enhancement. In: Unconventional resources technology conference, 13–15 June 2023. SEG Global Meeting Abstracts. Unconventional Resources Technology Conference (URTeC), pp 1453–1464
- Abdelaziz A, Grasselli G (2018) Investigating frictional behavior of micro-cracks using grain based modelling in the combined finite-discrete element method (FDEM). *OnePetro*, Richardson
- Aboyanah KR, Popoola AK, Sun L, Peterson K, Grasselli G (2021) Grain-based finite-discrete element modeling of thermal cracking in stanstead granite. In: ARMA/DGS/SEG 2nd international geomechanics symposium, pp ARMA-IGS-21-099
- Aboyanah KR, Popoola AK, Abdelaziz A, Sun L, Ossetchkina E, Peterson K, Grasselli G (2022) Effect of pre-existing cracks on thermal cracking of granitic rocks under confinement. *Geomech Geophys Geo-Energy Geo-Resour* 8(4):126
- Aboyanah KR, Sun L, Grasselli G (2023) Investigating thermal gradient cracking and fracture process zone development in granitic rocks. In: International geomechanics symposium, pp ARMA-IGS-2023-0289
- Aboyanah KR, Abdelaziz A, Haile BF, Zhao Q, Grasselli G (2024) Evaluation of damage stress thresholds and mechanical properties of granite: new insights from digital image correlation and GB-FDEM. *Rock Mech Rock Eng* 57:4679–4706
- Alm O, Jaktlund L-L, Shaoquan K (1985) The influence of microcrack density on the elastic and fracture mechanical properties of Stripa granite. *Phys Earth Planet Inter* 40(3):161–179
- ASM (1990) Properties and selection: nonferrous alloys and special-purpose materials. ASM International, Detroit
- Balme MR, Rocchi V, Jones C, Sammonds PR, Meredith PG, Boon S (2004) Fracture toughness measurements on igneous rocks using a high-pressure, high-temperature rock fracture mechanics cell. *J Volcanol Geotherm Res* 132(2):159–172
- Batarseh S, Gahan BC, Graves RM, Parker RA (2003) Well perforation using high-power lasers. In: SPE annual technical conference and exhibition, pp SPE-84418-MS
- Batarseh S, Mutairi S, San Roman Alerigi D, Al Harith A (2021) Laser technology for downhole applications: past, present and future. In: SPE Middle East oil and gas show and conference, pp D031S016R006
- Belrhit Y, Gallet-Doncieux A, Germaneau A, Doumalin P, Dupre JC, Alzina A, Michaud P, Pop IO, Huger M, Chotard T (2012) Application of optical methods to investigate the non-linear asymmetric behavior of ceramics exhibiting large strain to rupture by four-points bending test. *J Eur Ceram Soc* 32(16):4073–4081
- Bradski G, Kaehler A (2008) *Learning OpenCV: computer vision with the OpenCV library*. O'Reilly Media Inc, California
- Browning J, Meredith P, Gudmundsson A (2016) Cooling-dominated cracking in thermally stressed volcanic rocks. *Geophys Res Lett* 43(16):8417–8425
- Buscheck TA, Rosenberg ND, Gansemer J, Sun Y (2002) Thermohydrologic behavior at an underground nuclear waste repository. *Water Resour Res* 38(3):10-1–10-19
- Carlson SR, Jansen DP, Young RP (1993) Thermally induced fracturing of Lac du Bonnet granite. Report RP020AECL. Eng Seismol Lab, Queen's Univ, Kingston
- Chen T, Zheng X, Qiu X, Feng X-T, Elsworth D, Cui G, Jia Z, Pan Z (2021) Experimental study on the feasibility of microwave heating fracturing for enhanced shale gas recovery. *J Nat Gas Sci Eng* 94:104073
- Cho W-J, Kim J-S, Lee C, Kwon S, Choi J-W (2012) In situ experiments on the performance of near-field for nuclear waste repository at KURT. *Nucl Eng Des* 252:278–288
- Cooper HW, Simmons G (1977) The effect of cracks on the thermal expansion of rocks. *Earth Planet Sci Lett* 36(3):404–412
- Corr D, Accardi M, Graham-Brady L, Shah S (2007) Digital image correlation analysis of interfacial debonding properties and fracture behavior in concrete. *Eng Fract Mech* 74(1):109–121
- Cui G, Chen T, Feng X, Chen Z, Elsworth D, Yu H, Zheng X, Pan Z (2020) Coupled multiscale-modeling of microwave-heating-induced fracturing in shales. *Int J Rock Mech Min Sci* 136:104520
- Dong W, Wu Z, Zhou X, Wang N, Kastiukas G (2017) An experimental study on crack propagation at rock-concrete interface using digital image correlation technique. *Eng Fract Mech* 171:50–63
- Dutler N, Nejati M, Valley B, Amann F, Molinari G (2018) On the link between fracture toughness, tensile strength, and fracture process zone in anisotropic rocks. *Eng Fract Mech* 201:56–79
- Fan LF, Wu ZJ, Wan Z, Gao JW (2017) Experimental investigation of thermal effects on dynamic behavior of granite. *Appl Therm Eng* 125:94–103
- Fan LF, Gao JW, Wu ZJ, Yang SQ, Ma GW (2018) An investigation of thermal effects on micro-properties of granite by X-ray CT technique. *Appl Therm Eng* 140:505–519
- Feng G, Wang X, Kang Y, Zhang Z (2020) Effect of thermal cycling-dependent cracks on physical and mechanical properties of granite for enhanced geothermal system. *Int J Rock Mech Min Sci* 134:104476
- Fredrich JT, Wong T-F (1986) Micromechanics of thermally induced cracking in three crustal rocks. *J Geophys Res Solid Earth* 91(B12):12743–12764
- Freire-Lista DM, Fort R, Varas-Muriel MJ (2016) Thermal stress-induced microcracking in building granite. *Eng Geol* 206:83–93
- Gaucher E, Schoenball M, Heidbach O, Zang A, Fokker PA, van Wees JD, Kohl T (2015) Induced seismicity in geothermal reservoirs: a review of forecasting approaches. *Renew Sustain Energy Rev* 52:1473–1490
- Gautam PK, Singh SP, Agarwal A, Singh TN (2022) Thermomechanical characterization of two Jalore granites with different grain sizes for India's HLW disposal. *Bull Eng Geol Environ* 81(11):457
- Glover PWJ, Baud P, Darot M, Meredith PG, Boon SA, LeRavalec M, Zoussi S, Reuschlé T (1995) α/β phase transition in quartz monitored using acoustic emissions. *Geophys J Int* 120(3):775–782
- Griffiths L, Lengliné O, Heap MJ, Baud P, Schmittbuhl J (2018) Thermal cracking in Westerly granite monitored using direct wave velocity, coda wave interferometry, and acoustic emissions. *J Geophys Res Solid Earth* 123(3):2246–2261
- Gunatilake T (2023) Dynamics between earthquakes, volcanic eruptions, and geothermal energy exploitation in Japan. *Sci Rep* 13(1):4625

- Guo S, Dai Q, Sun X, Xiao X (2017) X-ray CT characterization and fracture simulation of ASR damage of glass particles in alkaline solution and mortar. *Theor Appl Fract Mech* 92:76–88
- Han Y, Fang Y, San-Roman-Alerigi DP, Batarseh SI (2019) Thermal/mechanical interaction in laser perforation process: numerical-model buildup and parametric study. *SPE J* 24(05):2097–2110
- Hassani F, Nekoovaght PM, Gharib N (2016) The influence of microwave irradiation on rocks for microwave-assisted underground excavation. *J Rock Mech Geotech Eng* 8(1):1–15
- Hassani F, Shadi A, Rafezi H, Sasmito AP, Ghoreishi-Madiseh SA (2020) Energy analysis of the effectiveness of microwave-assisted fragmentation. *Miner Eng* 159:106642
- Heap MJ, Lavallée Y, Petrakova L, Baud P, Reuschlé T, Varley NR, Dingwell DB (2014) Microstructural controls on the physical and mechanical properties of edifice-forming andesites at Volcán de Colima, Mexico. *J Geophys Res Solid Earth* 119(4):2925–2963
- Izadi G, Elsworth D (2015) The influence of thermal-hydraulic-mechanical- and chemical effects on the evolution of permeability, seismicity and heat production in geothermal reservoirs. *Geothermics* 53:385–395
- Jansen DP, Carlson SR, Young RP, Hutchins DA (1993) Ultrasonic imaging and acoustic emission monitoring of thermally induced microcracks in Lac du Bonnet granite. *J Geophys Res Solid Earth* 98(B12):22231–22243
- Jin P, Hu Y, Shao J, Zhao G, Zhu X, Li C (2019) Influence of different thermal cycling treatments on the physical, mechanical and transport properties of granite. *Geothermics* 78:118–128
- Johnson SE, Song WJ, Cook AC, Vel SS, Gerbi CC (2021) The quartz $\alpha \leftrightarrow \beta$ phase transition: does it drive damage and reaction in continental crust? *Earth Planet Sci Lett* 553:116622
- Just J, Kontny A (2012) Thermally induced alterations of minerals during measurements of the temperature dependence of magnetic susceptibility: a case study from the hydrothermally altered Soultz-sous-Forêts granite, France. *Int J Earth Sci* 101(3):819–839
- Kafashi S, Kuhar L, Bóna A, Nikoloski AN (2023) Review of fracturing techniques (microwaves, high-voltage pulses, and cryogenic fluids) for application as access creation method in low-permeability hard rocks for potential in situ metal recovery. *Miner Process Extract Metall Rev*. <https://doi.org/10.1080/08827508.2023.2196070>
- Kirchhoff G, Pompe W, Bahr HA (1982) Structure dependence of thermally induced microcracking in porcelain studied by acoustic emission. *J Mater Sci* 17(10):2809–2816
- Kong B, Li Z, Wang E (2018) Fine characterization rock thermal damage by acoustic emission technique. *J Geophys Eng* 15(1):1–12
- Korenaga J (2007) Thermal cracking and the deep hydration of oceanic lithosphere: a key to the generation of plate tectonics? *J Geophys Res Solid Earth* 112:B5
- Li Z, Wong LNY, Teh CI (2017) Low cost colorimetry for assessment of fire damage in rock. *Eng Geol* 228:50–60
- Li Z, Wong LNY, Teh CI (2020) Influence of thermal and mechanical loading on development of microcracks in granite. *Rock Mech Rock Eng* 53(5):2035–2051
- Li N, Zhang S, Wang H, Wu S, Zou Y, Ma X, Zhou T (2021a) Thermal shock effect on acoustic emission response during laboratory hydraulic fracturing in Laizhou granite. *Rock Mech Rock Eng* 54(9):4793–4807
- Li Q, Li X, Yin T (2021b) Effect of microwave heating on fracture behavior of granite: an experimental investigation. *Eng Fract Mech* 250:107758
- Lin Q, Labuz JF (2013) Fracture of sandstone characterized by digital image correlation. *Int J Rock Mech Min Sci* 60:235–245
- Lin Q, Yuan H, Biolzi L, Labuz JF (2014) Opening and mixed mode fracture processes in a quasi-brittle material via digital imaging. *Eng Fract Mech* 131:176–193
- Lin F, Feng X-T, Li S-P, Zhang J-Y, Su X-X, Tong T-Y (2023) Optimization of microwave presplitting iron ore to improve mechanical mining efficiency. *Rock Mech Rock Eng* 57:1897–1914
- Lisjak A, Mahabadi O, Ha J, Mas Ivars D (2023) Analysis of thermo-mechanical damage around tunnel and deposition boreholes of an underground nuclear waste disposal facility at the Forsmark site (Sweden) by 3D coupled FDEM simulations. *Int J Rock Mech Min Sci* 171:105586
- Liu W, Yang Y, Xia Q, Ye Y, Wang Z, Zhang P, Li G (2018) Water decreases displacive phase transition temperature in alkali feldspar. *Eur J Mineral* 30(6):1071–1081
- Liu J, Xue Y, Fu Y, Yao K, Liu J (2023) Numerical investigation on microwave-thermal recovery of shale gas based on a fully coupled electromagnetic, heat transfer, and multiphase flow model. *Energy* 263:126090
- Mahinpey N, Ambalae A, Asghari K (2007) In situ combustion in enhanced oil recovery (EOR): a review. *Chem Eng Commun* 194(8):995–1021
- Martínez-Garzón P, Kwiatak G, Sone H, Bohnhoff M, Dresen G, Hartline C (2014) Spatiotemporal changes, faulting regimes, and source parameters of induced seismicity: a case study from The Geysers geothermal field. *J Geophys Res Solid Earth* 119(11):8378–8396
- Meijering E, Jacob M, Sarria JC, Steiner P, Hirling H, Unser EM (2004) Design and validation of a tool for neurite tracing and analysis in fluorescence microscopy images. *Cytom A J Int Soc Anal Cytol* 58(2):167–176
- Meredith PG, Atkinson BK (1985) Fracture toughness and subcritical crack growth during high-temperature tensile deformation of Westerly granite and Black gabbro. *Phys Earth Planet Inter* 39(1):33–51
- Mo C, Zhao J, Zhang D (2022) Real-time measurement of mechanical behavior of granite during heating-cooling cycle: a mineralogical perspective. *Rock Mech Rock Eng* 55(7):4403–4422
- Mokheimer EMA, Hamdy M, Abubakar Z, Shakeel MR, Habib MA, Mahmoud M (2018) A comprehensive review of thermal enhanced oil recovery: techniques evaluation. *J Energy Resour Technol*. <https://doi.org/10.1115/1.4041096>
- Nasseri MHB, Schubnel A, Young RP (2007) Coupled evolutions of fracture toughness and elastic wave velocities at high crack density in thermally treated Westerly granite. *Int J Rock Mech Min Sci* 44(4):601–616
- Nasseri MHB, Tatone BSA, Grasselli G, Young RP (2009) Fracture toughness and fracture roughness interrelationship in thermally treated westerly granite. *Pure Appl Geophys* 166(5):801–822
- Nguyen TL, Hall SA, Vacher P, Viggiani G (2011) Fracture mechanisms in soft rock: identification and quantification of evolving displacement discontinuities by extended digital image correlation. *Tectonophysics* 503(1):117–128
- Nunez-Iglesias J, Blanch AJ, Looker O, Dixon MW, Tilley L (2018) A new Python library to analyse skeleton images confirms malaria parasite remodelling of the red blood cell membrane skeleton. *PeerJ* 6:e4312
- Olive J-A, Crone TJ (2018) Smoke without fire: how long can thermal cracking sustain hydrothermal circulation in the absence of magmatic heat? *J Geophys Res Solid Earth* 123(6):4561–4581
- Preibisch S, Saalfeld S, Tomancak P (2009) Globally optimal stitching of tiled 3D microscopic image acquisitions. *Bioinformatics* 25(11):1463–1465
- Rossi E, Kant MA, Madonna C, Saar MO, Rudolf von Rohr P (2018) The effects of high heating rate and high temperature on the rock strength: feasibility study of a thermally assisted drilling method. *Rock Mech Rock Eng* 51(9):2957–2964

- Rowland JV, Simmons SF (2012) Hydrologic, magmatic, and tectonic controls on hydrothermal flow, Taupo Volcanic Zone, New Zealand: implications for the formation of epithermal vein deposits. *Econ Geol* 107(3):427–457
- Scott S, Driesner T, Weis P (2015) Geologic controls on supercritical geothermal resources above magmatic intrusions. *Nat Commun* 6(1):7837
- Shao Z, Sun L, Aboyanah KR, Liu Q, Grasselli G (2022) Investigate the mode I fracture characteristics of granite after heating/-LN2 cooling treatments. *Rock Mech Rock Eng* 55:4477–4496
- Sun Q, Zhang W, Xue L, Zhang Z, Su T (2015) Thermal damage pattern and thresholds of granite. *Environ Earth Sci* 74:2341–2349
- Sun L, Liu Q, Grasselli G, Tang X (2020) Simulation of thermal cracking in anisotropic shale formations using the combined finite-discrete element method. *Comput Geotech* 117:103237
- Sun L, Tang X, Aboyanah KR, Zhao Q, Liu Q, Grasselli G (2023) A coupled cryogenic thermo-hydro-mechanical model for frozen medium: theory and implementation in FDEM. *J Rock Mech Geotech Eng*. <https://doi.org/10.1016/j.jrmge.2023.09.007>
- Taheri-Shakib J, Kantzas A (2021) A comprehensive review of microwave application on the oil shale: prospects for shale oil production. *Fuel* 305:121519
- Thirumalai K, Demou SG (1974) Thermal expansion behavior of intact and thermally fractured mine rocks. *AIP Conf Proc* 17(1):60–71
- Tian W-L, Yang S-Q, Elsworth D, Wang J-G, Li X-Z (2020) Permeability evolution and crack characteristics in granite under treatment at high temperature. *Int J Rock Mech Min Sci* 134:104461
- Todd TP (1973) Effect of cracks on elastic properties of low porosity rocks
- Van der Walt S, Schönberger JL, Nunez-Iglesias J, Boulogne F, Warner JD, Yager N, Gouillart E, Yu T (2014) scikit-image: image processing in Python. *PeerJ* 2:e453
- Van Rossum G, Drake FL (2009) Python 3 Reference Manual CreateSpace, Scotts Valley
- Veloso EE, Tardani D, Elizalde D, Godoy BE, Sánchez-Alfaro PA, Aron F, Reich M, Morata D (2020) A review of the geodynamic constraints on the development and evolution of geothermal systems in the Central Andean Volcanic Zone (18–28 Lat. S). *Int Geol Rev* 62(10):1294–1318
- Wang F, Konietzky H (2019) Thermo-mechanical properties of granite at elevated temperatures and numerical simulation of thermal cracking. *Rock Mech Rock Eng* 52(10):3737–3755
- Wang F, Konietzky H (2020) Thermal damage evolution of granite under slow and high-speed heating conditions. *Comput Geotech* 123:103590
- Wang F, Konietzky H (2022) Thermal cracking in granite during a heating-cooling cycle up to 1000 °C: laboratory testing and real-time simulation. *Rock Mech Rock Eng* 55:1411–1428
- Wang HF, Bonner BP, Carlson SR, Kowallis BJ, Heard HC (1989) Thermal stress cracking in granite. *J Geophys Res Solid Earth* 94(B2):1745–1758
- Wang F, Frühwirth T, Konietzky H, Zhu Q (2019) Thermo-mechanical behaviour of granite during high-speed heating. *Eng Geol* 260:105258
- Wang F, Konietzky H, Frühwirth T, Li Y, Dai Y (2020) Impact of cooling on fracturing process of granite after high-speed heating. *Int J Rock Mech Min Sci* 125:104155
- Wang D, Bian X, Qin H, Sun D, Yu B (2021) Experimental investigation of mechanical properties and failure behavior of fluid-saturated hot dry rocks. *Nat Resour Res* 30(1):289–305
- Wanne TS, Young RP (2008) Bonded-particle modeling of thermally fractured granite. *Int J Rock Mech Min Sci* 45(5):789–799
- Wong LNY, Zhang Y, Wu Z (2020) Rock strengthening or weakening upon heating in the mild temperature range? *Eng Geol* 272:105619
- Wu J, Gao J, Feng Z, Chen S, Nie T (2020) Investigation of fracture process zone properties of mode I fracture in heat-treated granite through digital image correlation. *Eng Fract Mech* 235:107192
- Wu F, Zhang D, Ma L, Meng T, Zhao G, Liu P, Zhang Z, Taherdangko R, Butscher C (2021) Thermo-hydro-mechanical (THM) evolution law and development of permeability and pore structure of enhanced geothermal systems at ultra-high temperatures. *Geothermics* 97:102253
- Xia M, Zhao C, Hobbs BE (2014) Particle simulation of thermally-induced rock damage with consideration of temperature-dependent elastic modulus and strength. *Comput Geotech* 55:461–473
- Xu JJ, Zhang YH, Rutqvist J, Hu MS, Wang ZZ, Tang XH (2023) Thermally induced microcracks in granite and their effect on the macroscale mechanical behavior. *J Geophys Res Solid Earth* 128(1):e2022JB024920
- Xu B, Huang X, Li B, Zhang B, Hu M, Ma C, Wang C, Liu T (2024) The effect of laser irradiation on the compressive strength of granite under uniaxial compression. *Rock Mech Rock Eng* 57:1881
- Xue Y, Liu S, Chai J, Liu J, Ranjith PG, Cai C, Gao F, Bai X (2023) Effect of water-cooling shock on fracture initiation and morphology of high-temperature granite: application of hydraulic fracturing to enhanced geothermal systems. *Appl Energy* 337:120858
- Yang S-Q (2022) Thermal damage and failure mechanical behavior of granite after exposure to different high temperature treatments under uniaxial compression. In: Yang S-Q (ed) *Mechanical behavior and damage fracture mechanism of deep rocks*. Springer Singapore, Singapore, pp 345–372
- Yang S-Q, Ranjith PG, Jing H-W, Tian W-L, Ju Y (2017) An experimental investigation on thermal damage and failure mechanical behavior of granite after exposure to different high temperature treatments. *Geothermics* 65:180–197
- Yong C, Wang CY (1980) Thermally induced acoustic emission in Westerly granite. *Geophys Res Lett* 7(12):1089–1092
- Yu P, Pan P-Z, Feng G, Wu Z, Zhao S (2020) Physico-mechanical properties of granite after cyclic thermal shock. *J Rock Mech Geotech Eng* 12(4):693–706
- Yuan H, Sun Q, Geng J, Tang L, Lv C, Zhang Y (2023) Thermal acoustic emission characteristics and damage evolution of granite under cyclic thermal shock. *Environ Earth Sci* 82(16):388
- Zhang W, Sun Q, Hao S, Geng J, Lv C (2016) Experimental study on the variation of physical and mechanical properties of rock after high temperature treatment. *Appl Therm Eng* 98:1297–1304
- Zhang W, Guo T-K, Qu Z-Q, Wang Z (2019) Research of fracture initiation and propagation in HDR fracturing under thermal stress from meso-damage perspective. *Energy* 178:508–521
- Zhang C, Feng Z, Mi C, Chen Z (2023) Experimental study on directional fracturing of granite by high-temperature thermal shock. *Rock Mech Rock Eng* 56(2):1199–1217
- Zhao Z (2016) Thermal influence on mechanical properties of granite: a microcracking perspective. *Rock Mech Rock Eng* 49(3):747–762
- Zhou C, Wan Z, Zhang Y, Gu B (2018) Experimental study on hydraulic fracturing of granite under thermal shock. *Geothermics* 71:146–155

Publisher's Note Springer Nature remains neutral with regard to jurisdictional claims in published maps and institutional affiliations.

Springer Nature or its licensor (e.g. a society or other partner) holds exclusive rights to this article under a publishing agreement with the author(s) or other rightsholder(s); author self-archiving of the accepted manuscript version of this article is solely governed by the terms of such publishing agreement and applicable law.